UNIVERSITY OF CALIFORNIA SAN DIEGO

Printed Indium Zinc Oxide Thin Film Transistors and Its Application as Photodetectors

A dissertation submitted in partial satisfaction of the requirements for the degree of Doctor of Philosophy

in

Materials Science and Engineering

by

Hyunwoong Kim

Committee in charge:

Professor Tse Nga Ng, Chair
Professor Shadi Dayeh
Professor Darren J. Lipomi
Professor Yu-Hwa Lo
Professor Paul Yu

2019

The Dissertation of Hyunwoong Kim is approved, and it is acceptable in quality and form for publication on microfilm and electronically:

_____

_____

_____

_____

_____
Chair

University of California San Diego

2019

DEDICATION

To my family

TABLE OF CONTENTS

LIST OF SYMBOLS AND ABBREVIATIONS

AOS	Amorphous oxide semiconductor
BV	Benzyl viologen
CA	1,7,7-trimethylbicyclo[2.2.1]heptan-2-one (±)-camphor
CB	Conduction band
EIS	Electrochemical impedance spectroscopy
EQE	External viiiemicon efficiency
h	Planck's constant
IGZO	Indium galium zinc oxide
IR	Infrared
IZO	Indium zinc oxide
LDR	Linear dynamic range
MOS	Metal oxide semiconductor
MOSFET	Metal oxide semiconductor field effect transistor
NIR	Near infrared
PT	Phototransistor
SWIR	Shortwave infrared
TCO	Transparent conducting oxide
TFT	Thin film transistor
TLM	Transmission line measurement
VB	Valence band

LIST OF FIGURES

LIST OF TABLES

ACKNOWLEDGMENTS

First, I would like to express my sincere gratitude to my advisor Prof. Tse Nga (Tina) Ng for her continuous support, guidance, trust, and patience she has shown to me during my Ph.D. She has set the tone not only as an advisor with an enormous knowledge and endless inspiration but also as a person with thoughtfulness. I am not able to imagine any better mentor for my Ph.D study.

Besides my advisor, I would like to thank my committee members, Prof. Paul Yu, Prof. Yu-Hwa Lo, Prof. Darren Lipomi, and Shadi Dayeh for their invaluable guidance and comments. Their every comment and suggestion have me be filled up with full of motivation.

I am also grateful to Prof. Kwon from Soonchunhyang University for helping me make a soft-landing on whole new field of inkjet-printing. My gratitude also goes to Subin Oh and Eui-Keun Choi for their detailed explanation, rapid feedbacks, and tireless maintenance.

I would like to acknowledge my lab mates, Dr. Zhenghui (Andy) Wu, Dr. Moran Amit, Dr. Weichuan Yao, Dr. Ning Li (Luis), Udit Parekh, Kaiping Wang, Yichen Zhai, and Ellie Sadatian. It has been my pleasure to work with them in an atmosphere of mutual assistance. Working experience with summer intern undergraduate students, Hsun Hao (Howard) Hsu, Brandon Fields, and Zhenhao Pan would be unforgettable.

I would like to acknowledge my colleagues and friends inside and outside UCSD. They have helped me in various ways and have supported me along the way.

Last but by no means least, my special gratitude goes out to my family for their selfless love and trust that have made me inspired and kept motivated. Without their unconditional love, I would have not triumphed over adversity during my Ph.D.

Chapter 2, in part, are the reprint of the material as it appears in the publication: Hyonwoong Kim and Tse Nga Ng, "Reducing trap states in printed indium zinc oxide transistors by doping with benzyl viololgen", *Adv. Elec. Mater*., 1700631 (2018). The dissertation author was the primary author of the paper.

Chapter 3, in part, are the reprint of the material submitted for publication: Hyonwoong Kim, Zhenghui Wu, Naresh Eedegurala, Jason D. Azoulay, and Tse Nga Ng, "Solution Processed Phototransistors Combining Organic Absorber and Charge Transporting Oxide for Visible to Infrared Light Detction", The dissertation author was the primary author of the paper.

VITA

2012	B.S., Chemical Engineering, Dankook University, Korea
2014	M.S., Chemical Engineering, Dankook University, Korea
2019	Ph.D., Materials Science and Engineering
	University of California San Diego, US

PUBLICATIONS

Hyonwoong Kim, Zhenghui Wu, Naresh Eedegurala, Jason D. Azoulay, and Tse Nga Ng, "Solution Processed Phototransistors Combining Organic Absorber and Charge Transporting Oxide for Visible to Infrared Light Detction", *Under review*

Zhenghui Wu, Yichen Zhai, Hyonwoong Kim, Jason Azoulay, and Tse Nga Ng, "Emerging designs and characterization guidelines for polymer-based infrared photodetectors", *Account of Chemical Research,* 51, 3144 (2018)

Hyonwoong Kim and Tse Nga Ng, "Reducing trap states in printed indium zinc oxide transistors by doping with benzyl viololgen", *Adv. Elec. Mater*., 1700631 (2018)

Kasra Sardashti, Kai-Ting Hu, Kechao Tang, Sangwook Park, Hyonwoong Kim, Shailesh Madisetti, Paul McIntyre, Serge Oktyabrsky, Shariq Siddiqui, Bhagawan Sahu, Noami Yoshida, Jessica Kachian, and Andrew Kummel, "Sulfur passivation for the formation of Si-terminated Al_2O_3/SiGe(001) interfaces", *Appl. Surf. Sci.*, 366, 455 (2016)

Sang Wook Park, Hyonwoong Kim, Evgueni Chagarov, Shariq Siddiqui, Bhagawan Sahu, Naomi Yoshida, Jessica Kachian, Randall Feenstra, and Andrew C. Kummel, "Chemically selective formation of Si–O–Al on SiGe(110) and (001) for ALD nucleation using H_2O_2(g)", *Surf. Sci.*, 652, 322 (2016)

Sang Wook Park, Tobin Kaufman-Osborn, Hyonwoong Kim, Shariq Siddiqui, Bhagawan Sahu, Naomi Yoshida, Adam Brandt, and Andrew C. Kummel, "Combined wet and dry cleaning of SiGe(001)", *J. Vac. Sci. Technol. A*, 33, 041403 (2015)

CONFERENCES

Kim, Hyunwoong, Ng, T.N., "Organic/Inorganic Hybrid Shortwave Infrared Phototransistors with Improved Detectivity, International meeting on information technology (IMID), Summer (2018)

Kim, Hyunwoong, Ng, T.N., "Investigation of Printed Contact Properties in TFTs", UCSD-KU Symposium, Fall (2017)

Kim, Hyunwoong, Ng, T.N., "Printed Contacts in Thin Film Transistors", Society of Photographic Instrumentation Engineers (SPIE) (2017)

ABSTRACT OF THE DISSERTATION

Printed Indium Zinc Oxide Thin Film Transistors and Its Application as Photodetectors

by

Hyunwoong Kim

Doctor of Philosophy in Materials Science and Engineering

University of California San Diego, 2019

Professor Tse Nga Ng, Chair

Amorphous semiconducting oxides are attractive alternatives to silicon for implementing thin-film transistors (TFTs) in large-area electronics, because of the oxide

xix emiconductor's promising electron mobility, optical transparency in the visible spectrum, and compatibility with low-cost solution processing. Due to these advantages, it has been widely utilized as active layer of active matrix in display.

Firstly, in chapter 2, we fabricate indium zinc oxide thin film transistor by inkjet printing. To enhance the semiconductor performance and stability, indium zinc oxide (IZO) is tuned by charge-transfer molecular doping on the film surface. An air-stable, strongly reducing molecule benzyl viologen (BV) is used to induce charge-transfer doping of the indium zinc oxide semiconductor in inkjet-printed thin-film transistors. The device mobility is improved from 5.8 ± 1.4 $cm^2(V \cdot s)^{-1}$ in the undoped devices and reached up to 8.7 ± 1.0 $cm^2(V \cdot s)^{-1}$ after BV treatment. Through measurement of frequency-dependent admittance and capacitance, we quantify the density of interface states, and show that interfacial trap density is four times lower in the BV-doped transistors compared to un-doped devices.

In chapter 3, we demonstrate high-performance infrared phototransistors that uses a broadband organic bulk heterojunction (BHJ) responsive from the visible to the infrared, from 500 nm to 1400 nm. The device structure is based on a bilayer transistor channel that decouples the photogeneration and charge transport, and thus enabling independent optimization of each process. The organic layer is improved by incorporating highly polarizable camphor to increase carrier lifetime, and IZO with high electron mobility is employed for rapid charge transport. The phototransistors achieve a dynamic range of

127 dB and reach detectivity up to 5×10^{12} Jones under low light condition around 20 nW/cm^2, which outperforms commercial germanium photodiodes in the spectral range below 1300 nm. The photodetector metrics are measured with respect to the temporal bandwidth, applied voltage, and incident light power. In particular, the frequency and light dependence of the phototransistor characteristics are analyzed to understand the change in photoconductive gain under different working conditions.

Chapter 1 Introduction

1.1 Fundamentals of Thin Film Transistors

A Thin film transistor (TFT) is one of field effect transistors (FETs) consisting of active semiconducting layer, dielectric material, source, drain, gate electrodes, and substrate. The active semiconductor acts as a current path between source and drain electrodes. Charge density in the channel is adjusted by capacitive control by gate electrode through dielectric material. The active semiconductor is either n-type or p-type depending on its dominant carrier type and high mobility is preferred to enable good carrier transporting behavior. Source and drain electrodes are required to have low injection barrier for majority carrier at the interface of electrodes and semiconductor. Electrons and holes are injected into channel from the source electrode, which means current flows from drain to source and source to drain for n-type and p-type devices, respectively. The gate voltage with respect to the voltage of the source electrode, V_{GS} adjusts charge density in the channel.

Accumulation takes place when the charge concentration of free carriers at the dielectric/semiconductor interface starts to surpass the number of the charge in bulk charge of the semiconductor. When the device is in accumulation mode, drain-source bias (V_{DS}) affects the voltage drop in the channel. Small V_{DS} with compared to V_G-V_T results in resistor-like behavior, known as the linear regime (**Figure 1.1(a)**). In this region,

current-voltage characteristics follow the Ohm's law. However, when a sufficiently large V_{DS} is applied, it induces a large voltage drop in the channel, resulting lower potential than the threshold voltage near the drain. This drop leads for the channel to pinch off (**Figure 1.1(b)**) carriers and enter the saturation region (**Figure 1.1(c)**).

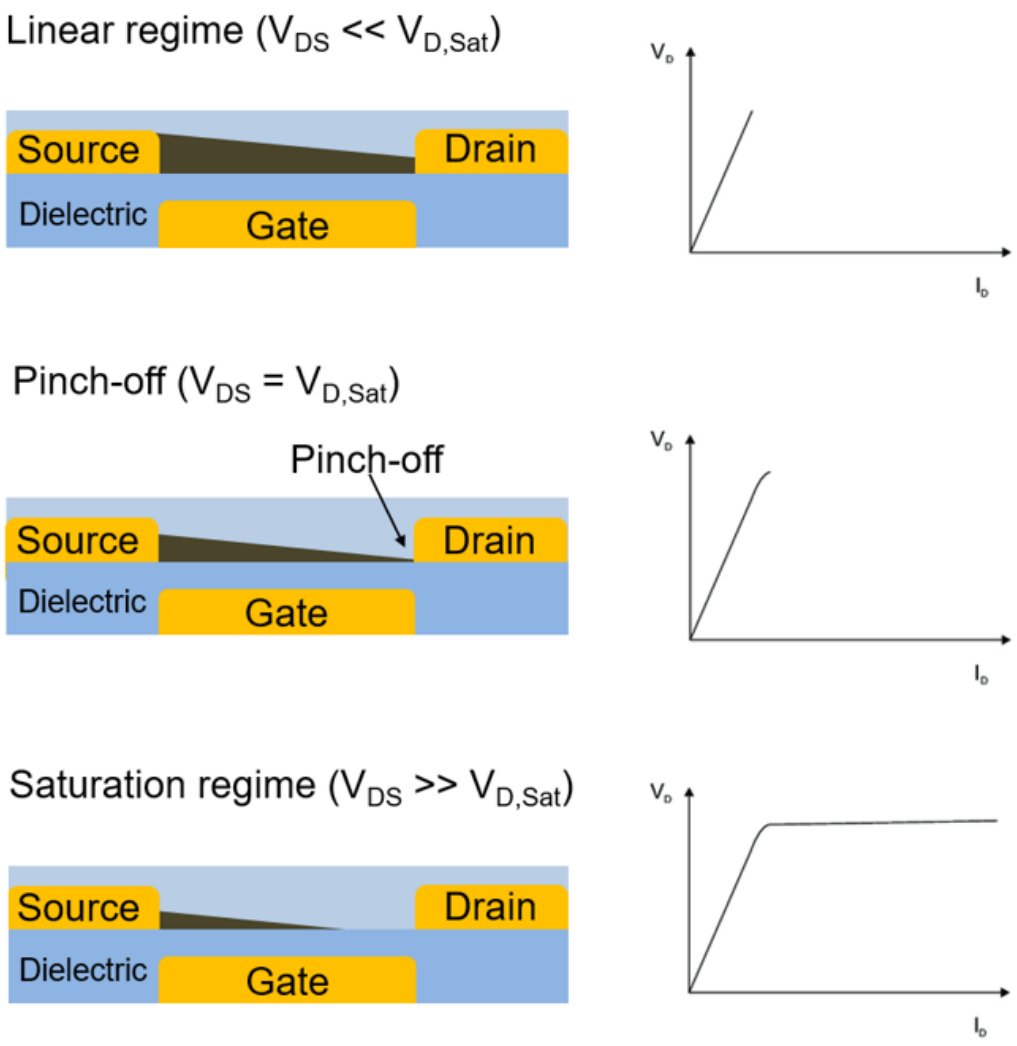

Figure 1.1. Schematic diagram illustrating channel formation in semiconductor active layer and resulting output characteristics at different operation regime.

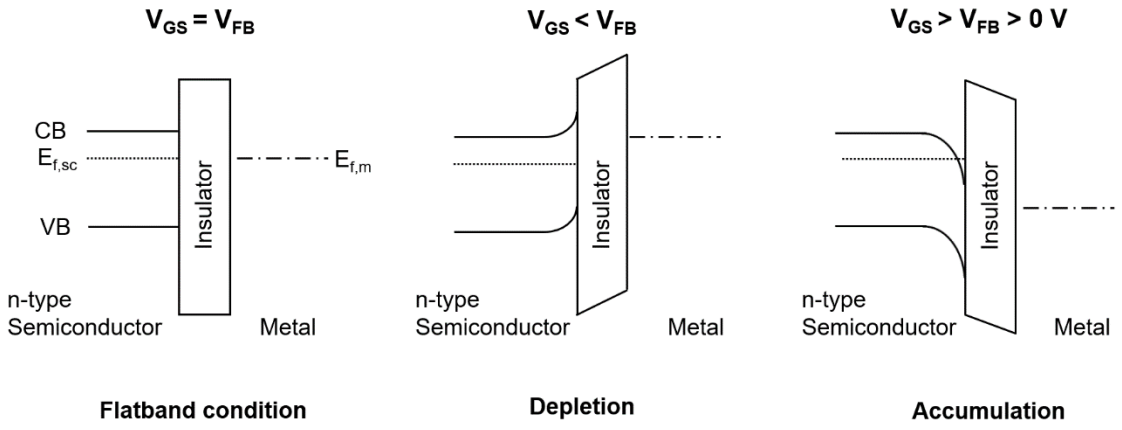

Figure 1.2. Energy band diagram of metal-oxide-semiconductor (MOS) at different gate bias condition. regime. Semiconductor is n-type in this schematic diagram.

As shown in **Figure 1.2**, change in gate voltage (V_{GS}) shifts the Fermi level and induces band bending. Band bending occurring dielectric/semiconductor interface modulates carrier charges at the interface.

Depending on the operation regime, current-voltage characteristics are divided into linear regime and saturation regime in thin film transistors. In each operation regime, equation describing in each regime is in the following.

Linear regime: $I_D = \frac{W}{L}\mu_n C_{ox}\left[(V_G - V_T)V_D - \frac{V_D^2}{2}\right]$, if $V_D << V_G - V_T$ (1-1)

Saturation regime: $I_{D,sat} = \frac{W}{2L}\mu_n C_{ox}(V_G - V_T)^2$, if $V_D >> V_G - V_T$ (1-2)

There are four device structures depending on the location of gate electrode and source/drain electrodes with respect to dielectric material and semiconductor.

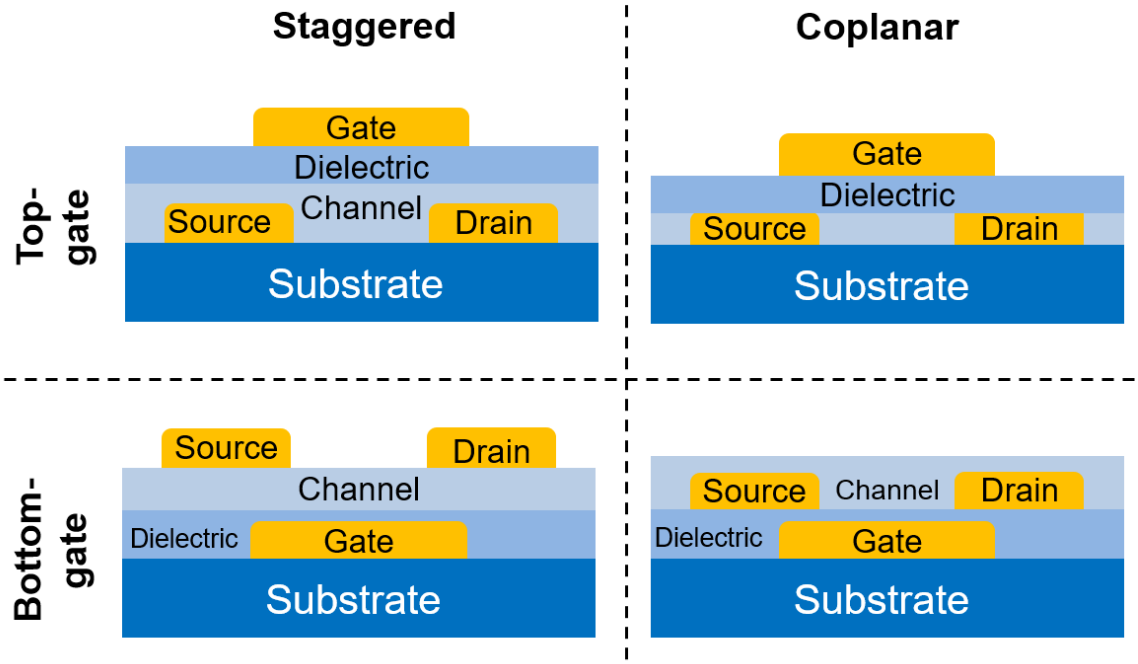

Figure 1.3. Four different device configurations based on the location of gate electrode and source/drain electrodes.

1.1.1 Gradual Channel Approximation

Gradual channel approximation is a model describing field effect transistor behavior. In gradual channel approximation, it is assumed that voltage varies gradually along the channel from the drain to source. To begin we assume that the voltage on the gate is sufficient to invert the channel.

When voltage is applied on source-drain electrodes and the source and the body are shorted, the voltage at source electrode and drain electrode is $V_{ch}(y=0)=0$ and $V_{ch}(y=L)=V_D$, respectively. Therefore, there is a variation in charge density in the inversion layer along the channel. In this calculation, it is assumed that $V_G-V_{ch}(y) > V_T$ throughout the channel hence there is a finite charge density everywhere in the channel. Under these conditions the depletion width is constant everywhere and the charge density along the channel of an n-channel MOSFET is,

$$Q(y) = -qn_s\mu_n E_{y=} - C_{ox}\{V_G - V_{ch}(y) - V_T\} \quad (1\text{-}3)$$

where $C_{ox}=\varepsilon_r\varepsilon_o/t_{ox}$ is the capacitance of the oxide per area. ε_r is the relative dielectric constant. ε_r is the permittivity constant, and tox is the thickness of the gate oxide. q is the electron elemental charge, n_s is the sheet charge density (electrons/m^2), μ_n is the electron mobility. Current density (j_y) is obtained as the following equation (1-4) since current density is proportional to the electric field,

$$j_y = nq\mu_n E_y \quad (1\text{-}4)$$

where n is the electron density (electrons/m^3) and μ_n is the electron mobility. The current flowing through channel is determined by multiplying the current density with the corresponding area, where W and t is the width and thickness of the channel, respectively.

$$I_D = Wtj = Wtn\mu_n E_y \quad (1\text{-}5)$$

Since $n_s=n\times t$, equation (1-5) becomes the following equation (1-6).

$$I_D = Wq\mu_n n_s(y)E_y(y) \tag{1-6}$$

Considering I_D is constant across the channel, the product $n_s(y)E_y(y)$ is also constant as a function of y. Therefore, the sheet charge decreases near the drain as the electric field increases near the drain. The sheet charge can be expressed by the following equation using the equation (1-3) for the charge in the inversion layer.

$$n_s(y) = -\frac{Q(y)}{q} = \frac{C_{ox}\{V_G - V_{ch}(y) - V_T\}}{q} \tag{1-7}$$

By inserting this expression for the sheet charge into the formula for the current one obtains,

$$I_D = W\mu_n C_{ox}\{V_G - V_{ch}(y) - V_T\}E_y \tag{1-8}$$

Since the electric field is negative derivative of the potential, $E_y = -dV_{ch}/dy$, E_y can be replaced with $-dV_{ch}/dy$ and it results in

$$I_D = -W\mu_n C_{ox}\{V_G - V_{ch}(y) - V_T\}\frac{dV_{ch}}{dy} \tag{1-9}$$

The electrons move towards the drain (in the y-direction) so the current is in the -y direction. It is conventional to take this as a positive drain current

$$I_D = W\mu_n C_{ox}\{V_G - V_{ch}(y) - V_T\}\frac{dV_{ch}}{dy} \tag{1-10}$$

Now, both sides can be integrated with the boundary condition of $V_{ch}=0$ at y=0 and $V_{ch}=V_D$ at y=L.

$$\int_0^L I_D dy = \int_0^{V_D} W\mu_n C_{ox}\{V_G - V_{ch}(y) - V_T\}dV \quad (1\text{-}11)$$

The current flowing from source to drain through is constant. Therefore, integration of the left side of equation (1-10) yields a factor of L. On the right side, all the parameters are constant except for V_{ch}(y). Therefore, integration results in the following expression for the drain current as a function of drain voltage (V_{DS}).

$$I_D = \frac{W}{L}\mu_n C_{ox}\left[(V_G - V_T)V_D - \frac{V_D^2}{2}\right] \quad (1\text{-}12)$$

This formula describes the relationship between drain current (I_D) and drain voltage (V_D) and it is valid until pinch-off point at drain electrode.

The current in the saturation region I_{sat} is the current that starts to appear in the linear regime at pinch-off as shown in **Figure 1.1**. At pinch-off point, it satisfies the condition of $dI_D/dV_D = 0$. In order to obtain V_{sat}, this condition can be applied on the equation (1-12).

$$\frac{dI_D}{dV_D} = \frac{W}{L}\mu_n C_{ox}[(V_G - V_T) - V_D] = 0 \quad (1\text{-}13)$$

In order to satisfy this condition, [(V_G-V_T)-V_D] needs to be zero. Hence, the saturation voltage (V_D,sat) is as follows.

$$V_{D,sat} = (V_G - V_T) \quad (1\text{-}14)$$

By substituting V_D in equation (1-12), the formula for the current in the linear regime, with V_G-V_T, the saturation current ($I_{D,sat}$) is determined as

$$I_{D,sat} = \frac{W}{2L}\mu_n C_{ox}(V_G - V_T)^2 \quad (1\text{-}15)$$

1.2 Oxide Semiconductors

1.2.1 Carrier Transport in Oxide Semiconductors

Oxide semiconductors, especially the amorphous ones, are a promising class of TFT materials that have made an impressive progress particularly in display applications in a relatively short time frame. Metal oxide semiconductors are composed of metal cations and oxygen anions. Oxide semiconductors possess wide band gap in which the *n*s orbitals of the HMCs primarily constitute the bottom part of the conduction band and the oxygen 2p orbitals form the top of the valence band.

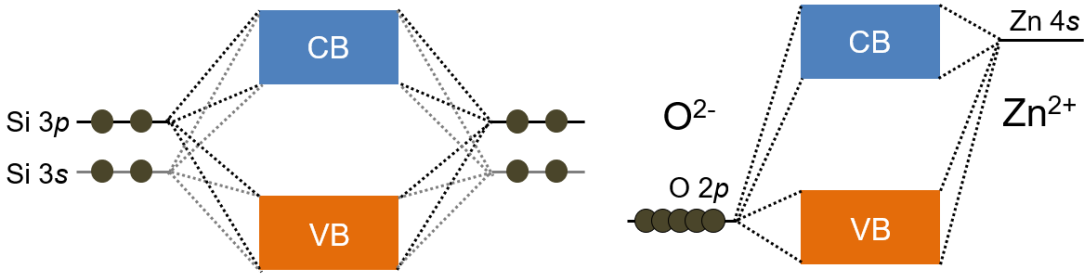

Figure 1.4. Schematic band structure of (left) silicon and (right) ZnO[1].

The electronic structures of most oxides are totally different from those of covalent semiconductors. In conventional covalent semiconductor, silicon, conduction band minimum (CBM) and valence band maximum (VBM) are composed of anti-bonding (sp^3 σ*) and bonding states (sp^3 σ) of silicon sp^3 hybridized orbitals and its bandgap is generated by the energy splitting of the σ*-σ levels[2]. In ionic oxides, CBM and VBM are usually formed by different ionic species. CBMs are mainly originated from the orbitals from the metal cations, Zn^{2+} 4s orbitals, and VBMs are mainly composed of O^{2-} 2p orbitals[3]. This is illustrated in **Figure in 1.4.**

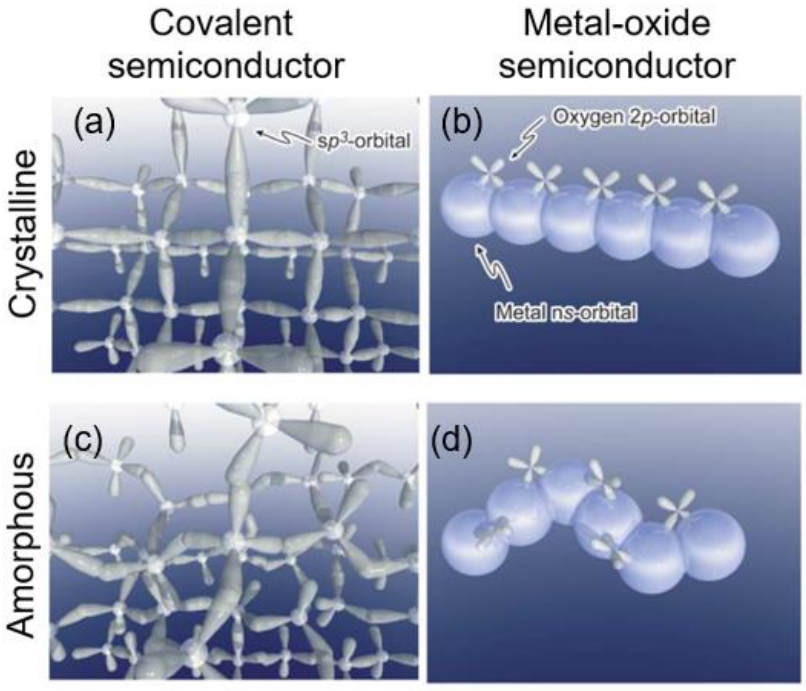

Figure 1.5. Schematic diagram of orbital structure showing crystalline of (a) silicon and (b) metal oxide semiconductor and amorphous of (c) silicon and (b) metal oxide semiconductor[3].

Normally, amorphous semiconductors exhibit much degraded carrier transport behavior than crystalline materials. This is attributed to the chemical bonds in the covalent semiconductors are composed of sp^3 orbitals that has high dependence on bonding direction. However, an amorphous oxide semiconductors (such as IZO[4], IGZO[5], SnO_2[6]), electrons transport through metal ion's *ns* orbital. Since ns orbital is in spherical shape, which is symmetrical, the conducting path and carrier mobility can be maintained even in amorphous state. To ensure high mobility in amorphous state, sufficient *ns* orbital overlap between metal ions is necessary.

Due to the advantage of amorphous oxide semiconductors, it has been widely used in display industry. Compared to silicon technology, which has been already mature stage, oxide semiconductors have advantages in its cost-effectiveness, large-area applicability, and mobility that is relatively insensitive to bonding angle distortion as shown in **Table 1.1.**

Table 1.1. Comparison of different TFT technology for displays

Material	Mobility [$cm^2v^{-1}s^{-1}$]	Transparency at Visible Light	Large Area Uniformity	Remarks
a-Si:H	<1	Poor	Good	Limiting current driving performance
Poly-Si	~100	Poor	Poor	Additional process is required for crystallization
ZnO	20-50	Good	Poor	Strong tendency to form poly phase
a-IGZO	3-12	Good	Good	Good balance in mobility and uniformity

1.2.2 Conventional Ionic Doping in Zinc Oxide Matrix

Conventional doping process has been an introduction of impurities into the lattice of semiconducting materials to tune the electrical properties. There have been many attempts to introduce different elements in the zinc oxide (ZnO) matrix to enhance its performance and stability. Park et al. has reported alkali metal (e.g. Li, Na, K, Rb) doped ZnO TFTs and found optimal concentration for carrier transfer.[7] Beyond certain concentration of dopants, excess dopant generates defects rather than doping. Do et al. has examined the influence of titanium doping on zinc tin oxide (ZTO) TFTs.[8] In their study, titanium atom was incorporated to adjust threshold voltage and reduce the oxygen vacancy in the ZTO film. Seo et al. has employed fluorine atom in their zinc oxide TFTs to substitute oxygen sites with doped fluorine atom and to reduce oxygen vacancies, resulting in improvement in device stability.[9] Henneck et al. has conducted systematical investigation on the effect of 'oxygen getter' ions in quaternary IXZO (X= Ga, Sc, Y, La).[10] They compared the device performance with undoped IZO and they studied the effect of incorporation of dopant on charge transport. Most of doping studies have been conducted to improve the device stability by suppressing the generation of oxygen vacancies and to enhance the carrier mobility.

As another approach of doping, charge transfer doping has been used due to an advantage over conventional substitutional doping in that it does not induce defect sites

and strain.[11-12] Charge transfer molecules spontaneously transfer carriers to an acceptor material, resulting from the difference in redox potential.

1.3 References

(1) Mashayekhi, M.; Conde, A.; Ng, T. N.; Mei, P.; Ramon, E.; Martinez-Domingo, C.; Alcalde, A.; Teres, L.; Bordoll, J. C. Inkjet Printing Design Rules Formalization and Improvement. *IEEE/OSA J. Disp. Technol.* **2015**, *11*, 658–665.

(2) Kamiya, T.; Hosono, H. Electronic Structures and Device Applications of Transparent Oxide Semiconductors: What Is the Real Merit of Oxide Semiconductors? *Int. J. Appl. Ceram. Technol.* **2005**, *2*, 285–294.

(3) Yu, X.; Marks, T. J.; Facchetti, A. Metal Oxides for Optoelectronic Applications. *Nat. Mater.* **2016**, *15*, 383.

(4) Kim, H.; Ng, T. N. Reducing Trap States in Printed Indium Zinc Oxide Transistors by Doping with Benzyl Viologen. *Adv. Electron. Mater.* **2018**, *4*, 1700631.

(5) Nomura, K.; Ohta, H.; Takagi, A.; Kamiya, T.; Hirano, M.; Hosono, H. Room-Temperature Fabrication of Transparent Flexible Thin-Film Transistors Using Amorphous Oxide Semiconductors. *Nature* **2004**, *432*, 488.

(6) Idota, Y.; Kubota, T.; Matsufuji, A.; Maekawa, Y.; Miyasaka, T. Tin-Based Amorphous Oxide: A High-Capacity Lithium-Ion-Storage Material. *Science (80-.).* **1997**, *276*, 1395–1397.

(7) Park, S. Y.; Kim, B. J.; Kim, K.; Kang, M. S.; Lim, K. H.; Lee, T. Il; Myoung, J. M.; Baik, H. K.; Cho, J. H.; Kim, Y. S. Low-Temperature, Solution-Processed and Alkali Metal Doped Zno for High-Performance Thin-Film Transistors. *Adv. Mater.* **2012**, *24*, 834–838.

(8) Do, J. C.; Ahn, C. H.; Cho, H. K.; Lee, H. S. Effect of Ti Addition on the Characteristics of Titanium-Zinc-Tin-Oxide Thin-Film Transistors Fabricated via a Solution Process. *J. Phys. D. Appl. Phys.* **2012**, *45*, 225103.

(9) Seo, J.-S.; Jeon, J.-H.; Hwang, Y. H.; Park, H.; Ryu, M.; Park, S.-H. K.; Bae, B.-S. Solution-Processed Flexible Fluorine-Doped Indium Zinc Oxide Thin-Film Transistors Fabricated on Plastic Film at Low Temperature. *Sci. Rep.* **2013**, *3*, 2085.

(10) Hennek, J. W.; Smith, J.; Yan, A.; Kim, M. G.; Zhao, W.; Dravid, V. P.; Facchetti, A.; Marks, T. J. Oxygen "Getter" Effects on Microstructure and Carrier Transport in Low Temperature Combustion-Processed a-InXZnO (X = Ga, Sc, Y, La)

Transistors. *J. Am. Chem. Soc.* **2013**, *135*, 10729–10741.

(11) Yu, S. H.; Kim, B. J.; Kang, M. S.; Kim, S. H.; Han, J. H.; Lee, J. Y.; Cho, J. H. In/Ga-Free, Inkjet-Printed Charge Transfer Doping for Solution-Processed ZnO. *ACS Appl. Mater. Interfaces* **2013**, *5*, 9765–9769.

(12) He, Y.; Xia, F.; Shao, Z.; Zhao, J.; Jie, J. Surface Charge Transfer Doping of Monolayer Phosphorene via Molecular Adsorption. *J. Phys. Chem. Lett.* **2015**, *6*, 4701–4710.

Chapter 2 Reducing Trap States of Printed Indium Zinc Oxide Thin Film Transistor by Doping with Benzyl Viologen

2.1 Abstract

An air-stable, strongly reducing molecule benzyl viologen (BV) is used to induce charge-transfer doping of the indium zinc oxide semiconductor in inkjet-printed thin-film transistors. The device mobility is improved from 5.8 ±1.4 $cm^2(V \cdot s)^{-1}$ in the undoped devices and reached up to 8.7 ±1.0 $cm^2(V \cdot s)^{-1}$ after BV treatment. Through measurement of frequency-dependent admittance and capacitance, this work quantifies the density of interface states, and shows that interfacial trap density is four times lower in the BV-doped transistors compared to un-doped devices.

2.2 Introduction

Amorphous semiconducting oxides[1,2] are attractive alternatives to silicon for implementing thin-film transistors (TFTs) in large-area electronics, because of the oxides' promising electron mobility, optical transparency in the visible spectrum, and compatibility with low-cost solution processing.[3–5] To enhance the semiconductor performance and stability, indium zinc oxide (IZO) and its variants have been tuned by ionic doping in the bulk or by charge-transfer molecular doping on the film surface. Ionic dopants over a wide range of atomic radii are shown to reduce oxygen vacancies in the

oxide films.[6,7] While ionic doping incorporates dopants throughout the film, doping based on charge-transfer molecules[8–11] occurs at the surface, where charge carriers are transferred due to a difference in redox potentials between the charge-transfer molecules and the film material. The molecules can be patterned, for example by inkjet printing, to selectively dope specific interfaces in TFTs. Molecular doping on oxides offers the advantage of local tuning but are not well studied, probably due to the tendency of organic dopants to degrade when exposed to air. **Figure 2.1** shows charge transfer doping behavior with the combination of charge transfer molecule, benzyl viologen, and metal oxide semiconductor, indium zinc oxide (IZO).

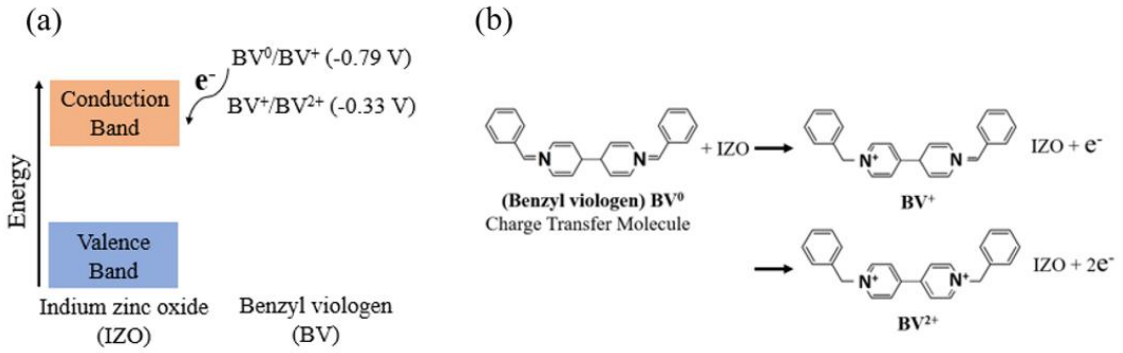

Figure 2.1. (a) Energy band diagram of indium zinc oxide and BV redox states. The conduction band edge of IZO is lower than the redox potential of the BV molecules. This energy level offset leads to electron donation from BV molecules to IZO. (b) Redox reactions of the BV molecule when it is applied on an acceptor material, IZO.

In this work, we chose an air-stable, strongly reducing molecule benzyl viologen (BV) to apply on IZO TFTs and investigated the effects of BV doping on interfacial states and transistor performance. The BV doping process allows ambient preparation and

shortens fabrication time, in contrast to prior approaches based on air-sensitive fullerene derivatives[12] or the slow formation of self-assembled monolayers.[13] The contact resistance before and after doping are compared by transmission-line method. In addition to typical current-voltage characteristics, the devices are characterized through capacitance and admittance measurements as a function of frequency and applied bias, to gain insights into charge transport affected by trap sites. Analyses of the cutoff frequency and the parallel conductance reveal the effective mobility and the density of trap states, respectively, for comparisons of un-doped and BV-doped TFTs. The Cole-Cole plot, based on the real and imaginary components of admittance, provides additional graphical analyses to understand the effect of BV treatment on interfacial states.

2.3 Experimental Procedures

All the patterning steps were performed by using inkjet printing.[14–16] For substrate preparation, a heavily doped p-type silicon wafer with 300 nm oxide layer was cleaned with acetone and 2-propanol and treated with UV-ozone for 5 min. The IZO ink[17] was prepared by dissolving 0.06 M of indium nitrate hydrate and 0.04 M of zinc nitrate hexahydrate in 2-methoxyethanol. The IZO precursor solution was deposited using an inkjet printhead (Fujifilm Dimatix DMP2800) with the substrate heated at 60°C. The printed IZO was annealed at 400°C in air for 2 hours. Subsequently to passivate the channel area, a solution of poly-4-vinylphenol (PVP) was printed and cross-linked at 160°C for 30 min. This PVP layer also served to confine BV doping to areas around the

electrodes; otherwise doping the entire TFT channel led to low on/off ratio due to inability to reach depletion.

The BV solution was prepared following the solvent exchange procedure in Ref. [10]. The un-ionized BV dissolved in toluene (concentration below 25 mg/ml) was spin-coated to dope the exposed areas not covered by PVP. Charge transfer between BV and IZO oxidized the BV^0 to BV^{2+} state. The IZO surface was rinsed with toluene to remove any excess un-ionized BV. The source and drain electrodes were printed with silver nanoparticle ink (Colloidal Inc.) as 250 μm by 250 μm pads and annealed at 150°C for an hour to complete the IZO TFTs. In the above analyses, the TFTs had channel width (W) of 180 μm and channel length (L) of 250 μm, unless indicated otherwise such as for the devices measured in transmission-line model. Devices were measured in the dark ambient, using Keithley Sourcemeter 2400 and Picoammeter 6438 for current-voltage characteristics, and Agilent Parameter Analyzer B1500 for frequency-dependent capacitance and admittance. In frequency-dependent measurements, the source and drain electrodes were connected together for measuring the electrode-insulator-semiconductor junction from 1 kHz to 2 MHz. The amplitude of ac voltage was 100 mV as dc voltage was swept between ±25 V.

2.4 Results and Discussions

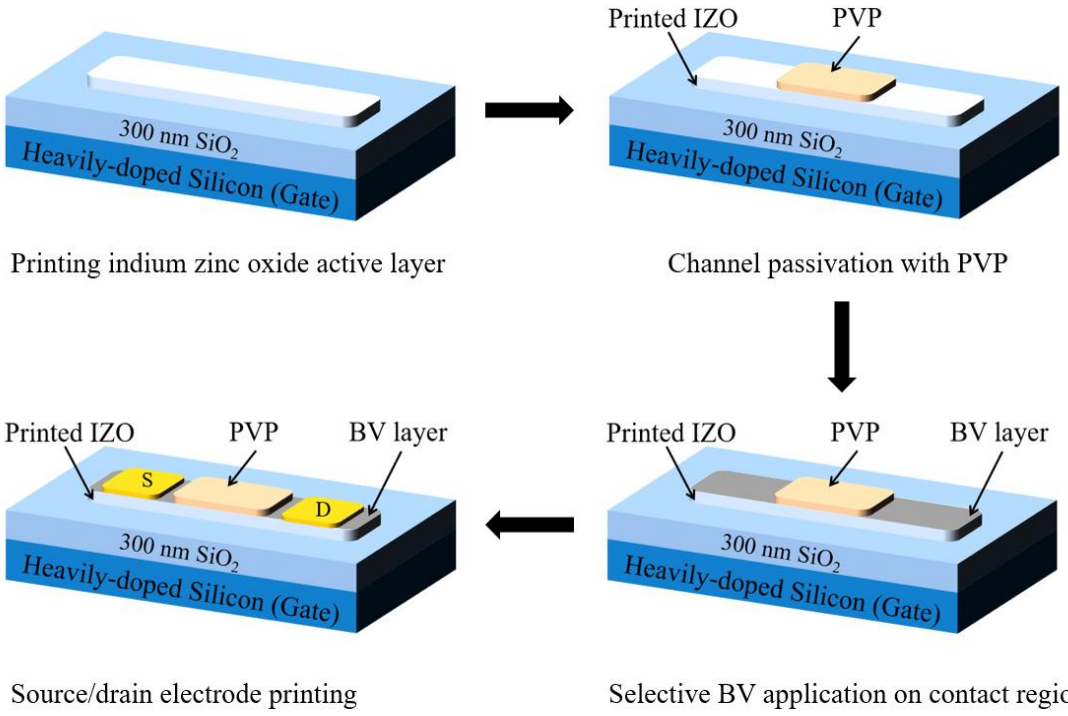

Figure 2.2. Fabrication process of printed IZO TFT with selective application of BV on contact region.

Figure 2.2 shows the device structure in a bottom-gate, top-contact configuration with doped source/drain electrodes with BV molecules [shown in **Figure 2.3(a)**]. The IZO semiconductor was deposited by inkjet, and the channel region was subsequently covered by an insulator polymer poly-4-vinylphenol. A BV solution was spin-coated onto the exposed areas, followed by a rinse with toluene to remove excess, not-ionized BV molecules. The BV treatment did not add measurable thickness, but the doping process increased wetting between the polar Ag ink and the IZO surface with ionized BV

molecules. Silver ink on untreated IZO showed a contact angle of approximately 30 degree, whereas the same Ag ink completely dispersed on the BV-treated surface, as seen in the photographs of **Figure 2.3(b), (c)**.

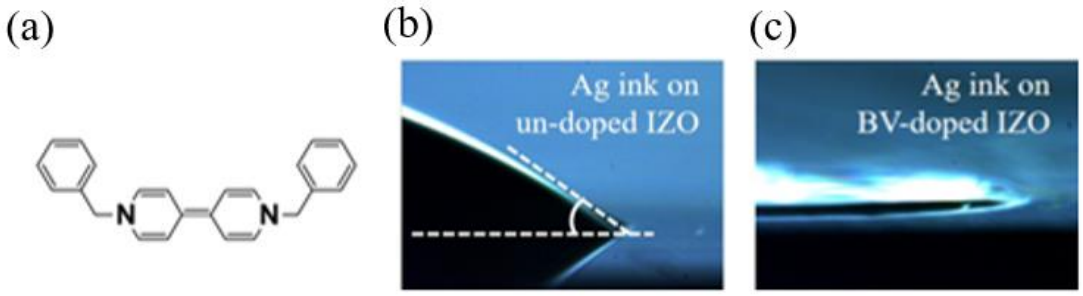

Figure 2.3. (a) Chemical structure of benzyl viologen (BV) in the reduced state. (b, c) Photographs of the contact angle between Ag ink on un-doped IZO and on BV-doped IZO.

Figure 2.4 shows typical transfer and output characteristics of un-doped and BV-doped TFTs. The BV-doped TFT shows a more negative threshold voltage and a higher off-current than the un-doped TFT. If the entire channel is doped, the IZO becomes very conductive, and the applied electric field is not sufficient to modulate and depletes the channel. Hence we restricted BV doping to areas underneath the source and drain contacts. There is a possibility that our process may allow the BV solution to wick underneath the PVP barrier and partially dope the channel region. However, the more likely explanation for the negative shift in threshold voltage is that the IZO layer is relatively thick at around 30 nm, and as such the BV doping leads to a very conductive area underneath the contacts that are difficult to deplete.

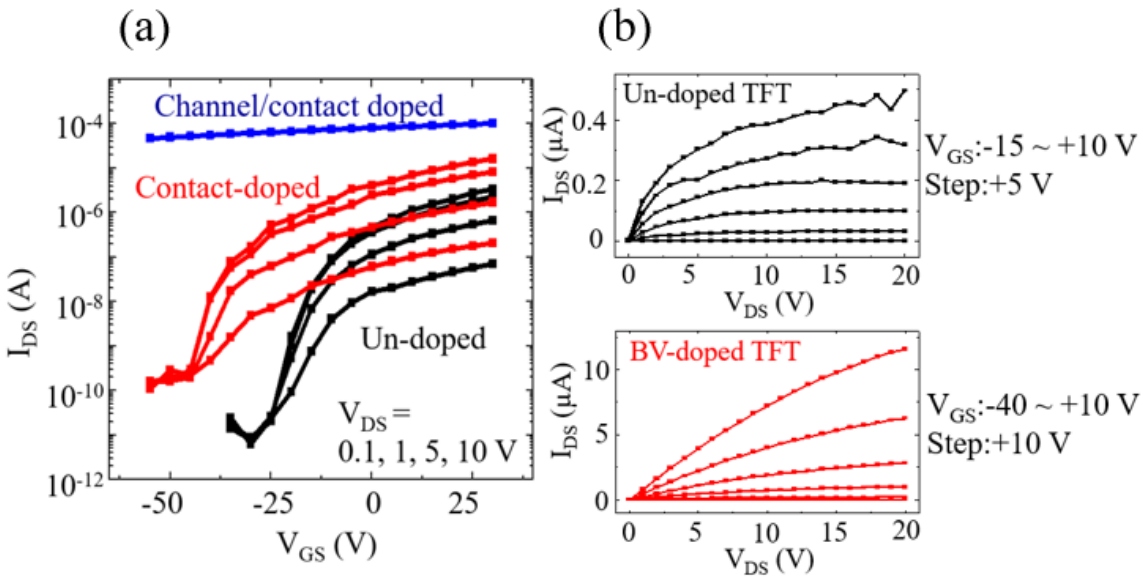

Figure 2.4. (a) Transfer and (b) output characteristics. Un-doped TFT: black. BV-doped TFT: red. The blue curve in (a) is the transfer characteristics at V_{DS}=10 V of a device where both the channel and contact regions are doped.

The field-effect mobility μ is determined from the slope of the transfer curve at saturation by

$$I_{DS} = (W/L)(C_g \mu (V_{GS} - V_{th})^2)/2 \qquad (2\text{-}1)$$

where I_{DS} is the source-drain current, W is the channel width, L is the channel length, C_g is the gate dielectric capacitance, V_{GS} is the applied gate bias, and V_{th} is the threshold voltage. The average mobilities of ten devices are 5.8 ±1.4 $cm^2(V \cdot s)^{-1}$ for un-doped TFTs and 8.7 ±1.0 $cm^2(V \cdot s)^{-1}$ for BV-doped TFTs. The variations in transfer characteristics are shown in **Figure 2.5**.

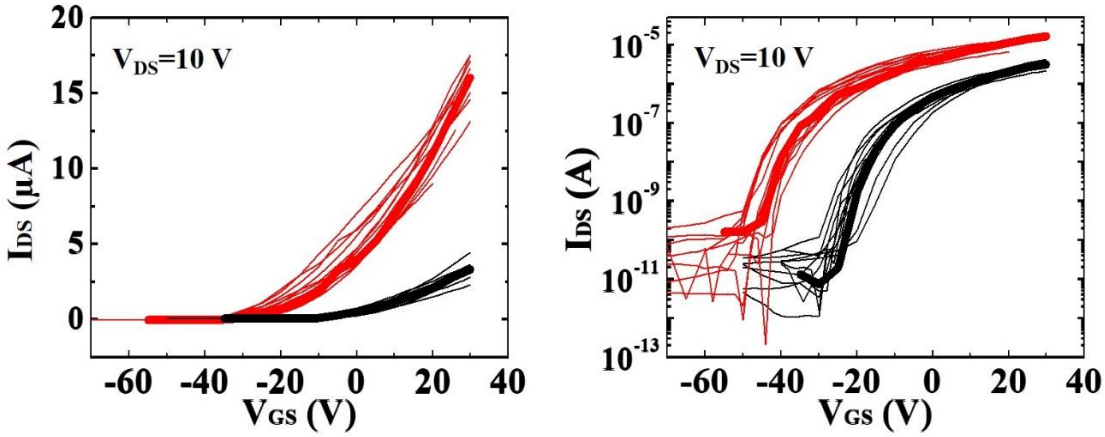

Figure 2.5. Transfer characteristics of 12 devices each for the BV-doped (red) and un-doped (black) thin-film transistors. The bold lines indicate the representative device analyzed in the main manuscript.

Typical bias stress measurements in **Figure 2.6 (a)** shows slower decay in drain-source current in the BV-doped TFT than the un-doped device. The contact resistance of the BV-doped TFTs are extracted using transmission line method,[18] where the output device resistance is expressed as $dV_{DS}/dI_{DS} = r_{ch}L + R_c$, where $r_{ch}L$ is the channel resistance and R_c is the sum of the contact resistance of both source and drain electrodes. The series of dV_{DS}/dI_{DS} data versus channel length L allow extrapolation to determine the contact resistance R_c, which is the y-intercept in **Figure 2.6(b)**. The contact resistance of BV-doped contacts is 153 kΩ, compared to 3.47 MΩ for un-doped contacts at gate bias of 0 V. In addition to contact resistance, the devices are further examined below by capacitance and conductance analyses to clarify why BV treatment improves mobility and stability.

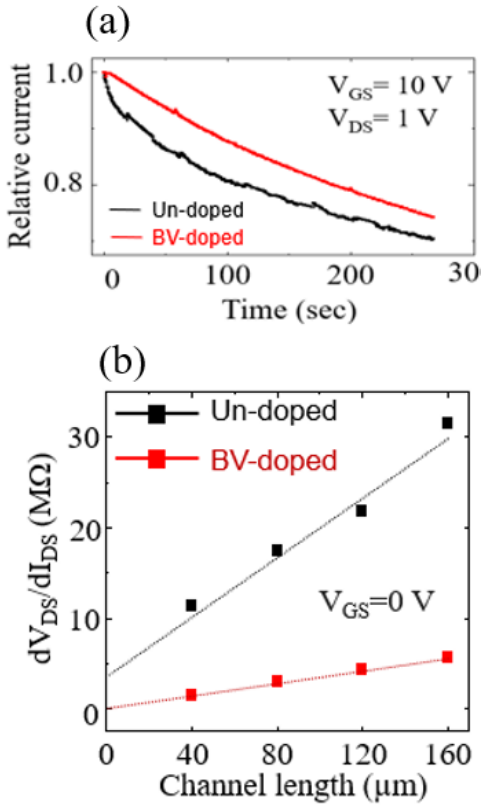

Figure 2.6. (a) Bias stress measurements. Un-doped TFT: black. BV-doped TFT: red. (b) Device resistance versus channel length, in which the y-intercept denotes the contact resistance based on transmission line model.

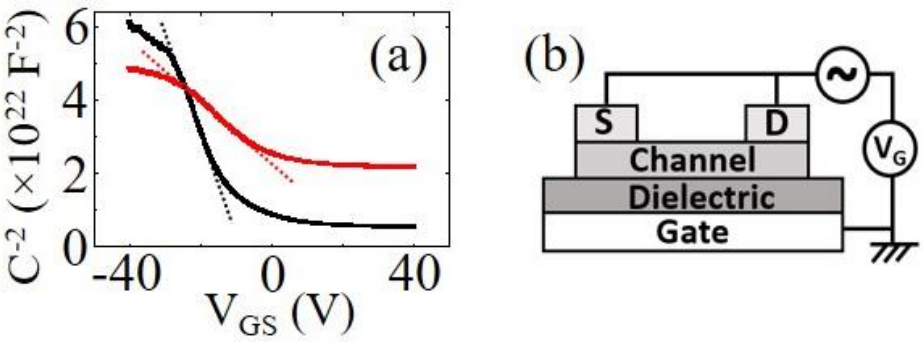

Figure 2.7. (a) Mott-Schottky plot at 5 kHz. (b) Measurement schematics. Un-doped TFT: black. BV-doped TFT: red.

The dopant concentration of BV in IZO is estimated from the measured capacitance C_m with respect to varying gate bias in **Figure 2.7**, by fitting to the Mott-Schottky relation $\partial(1/C_m^2)/\partial V_{GS} = 2/(q\varepsilon_o\varepsilon_s N_D A^2)$, where q is the electronic charge, ε_o is the permittivity of vacuum, ε_s =8.5 is the relative permittivity of IZO, N_D is the dopant concentration, and A is the semiconductor area of 0.183 mm by 1.13 mm here. The error of the area can be up to 10% with our optical microscope measurement, but the semiconductor area, channel W and L, and the electrode areas are the same for both undoped and contact-doped devices. Dopant concentration N_D is estimated to be 3.0×10^{17} cm^{-3} after the BV treatment, whereas un-doped device shows 1.5×10^{17} cm^{-3}. The rise in N_D value confirms electron transfer from BV molecules to IZO semiconductor**.**

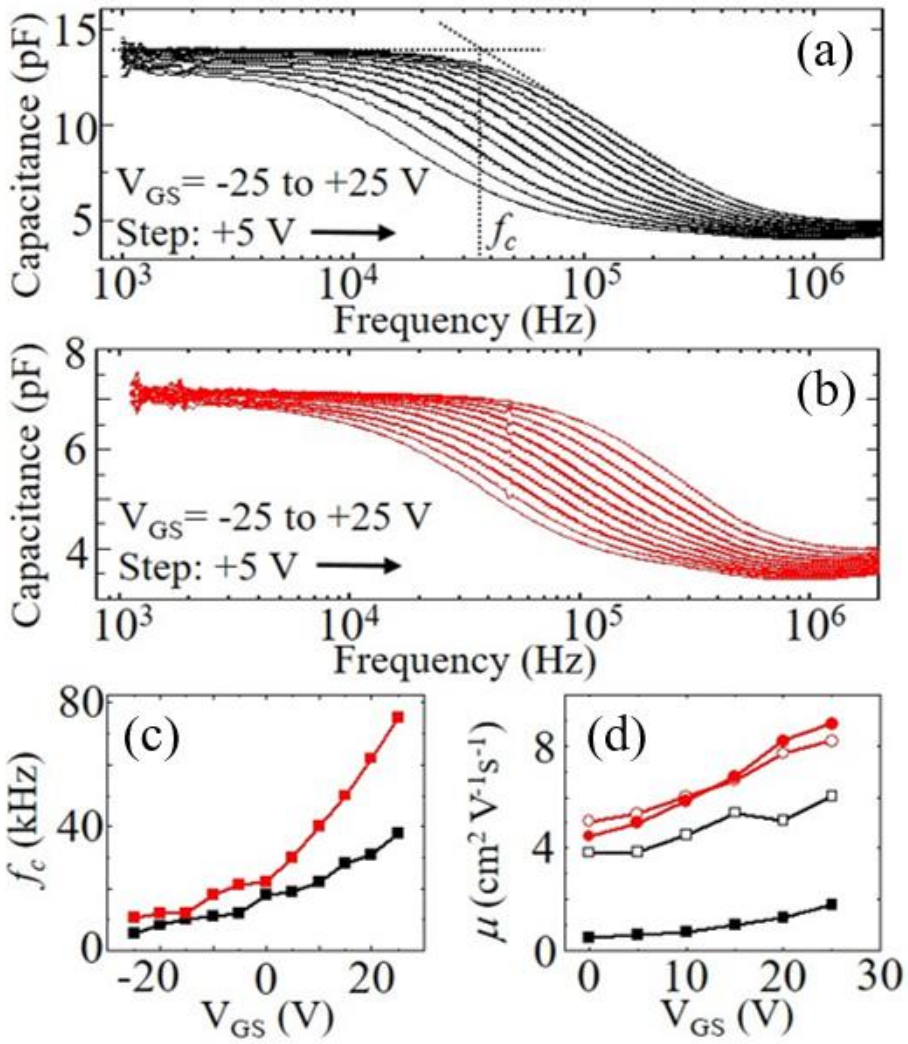

Figure 2.8. Capacitance as a function of frequency for (a) un-doped, (b) BV-doped IZO TFTs. (c) Cutoff frequencies for un-doped and BV-doped devices. (d) Mobilities estimated from cutoff frequencies (solid symbols) and current-voltage characteristics (open symbols). Un-doped TFT: black. BV-doped TFT: red.

Besides increasing the dopant concentrations in IZO, the BV treatment increases the cutoff frequency, as the devices are biased in the voltage range for charge

accumulation. Cutoff frequencies were determined from the intersection points where capacitance started to decrease as shown in **Figure 2.8(a)-(c)**. The cutoff frequency f_c at each gate bias is correlated to the field-effect mobility by the following equation[19]:

$$\mu = 2\pi L^2 f_c / (V_{GS} - V_{th}) \tag{2-2}$$

For the amorphous IZO devices, the mobility improves with BV doping. The measurement probed the interfaces of the IZO channel and the contact areas under the doped electrodes. Our model cannot separate the two types of interfaces. Nonetheless, the capacitance measurement showed that there was a two times increase in carrier concentration due to BV doping, and the increased free carrier concentration filled up the trap state and led to a transition from trap-limited conduction to percolation transport[20] across the device channel. Thereby the excess carriers beyond the bandtail show better charge transport.

Figure 2.8(d) compares the field-effect mobilities inferred from the current-voltage (I-V) characteristics (**Equation 1**) and from the cutoff frequency (**Equation 2**). The BV-doped TFT shows similar mobility using the two different measurement methods. However, the un-doped TFT shows a discrepancy where the value from I-V characteristics is higher than that of capacitance-frequency (C-f) measurements. This difference is attributed to the bias stress effect, namely, a reduction in device current as mobile carriers fell into trap states during device operation.[21,22] Gate bias was applied for

a longer time in C-f measurement (sampled at 0.12 second per point, total 2,200 data points) than in I-V characterization (0.5 second per point, total 72 data points). Thus, TFTs were more severely affected by bias stress in C-f measurement.

The un-doped device is more affected by bias stress, and its capacitance is also higher than that of the BV-doped TFT. The device capacitance at the low frequency regime is influenced by the capacitance of dielectric layer, the interfacial charges, and the depletion capacitance of the IZO/dielectric junction. When operating in accumulation mode, the depletion capacitance is negligible. Since we measure the devices to have the same dielectric capacitance, the main factor that explains the high capacitance in un-doped TFTs is an increase in the number of interfacial charges that are located in bandtail trap states.

To quantify the density of interfacial trap states, we use the admittance method which models the loss in conductance due to the trap capture and emission processes. As the conductance change is directly measured, the admittance method eliminates the need for extensive fitting as is the case when using capacitance data. The maximum conductance loss occurs when the trapping process is in resonance with the probing frequency at an applied bias, i.e., when the energy level of trap states is aligned with Fermi level of semiconductor. Therefore, the admittance method is accurate for estimating the density of traps within ~100 mV (a few constants of k_BT/q, where k_B is the Boltzmann's constant and T is the temperature) adjacent to the Fermi level.[23]

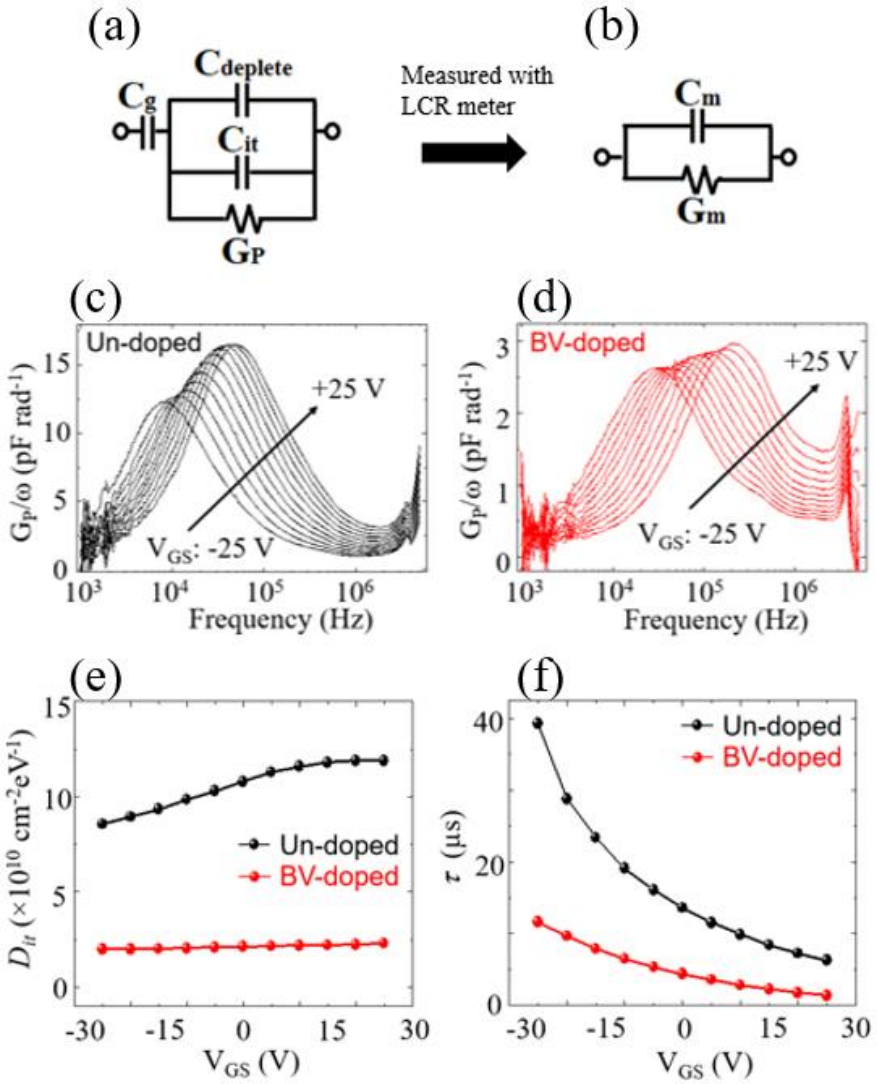

Figure 2.9. (a) Equivalent circuit model of the MOS capacitor, where the parallel conductance G_p, the interface states capacitance C_{it}, and the depletion capacitance $C_{deplete}$ are in parallel, and the above components are in series with the gate dielectric capacitance C_g. (b) Equivalent circuit as seen by the impedance analyzer, where the measured conductance G_m and measured capacitance C_m are in parallel. Frequency dependence of G_P/ω for (c) un-doped (d) BV-doped TFTs. The gate biases are increased from -25 V to 25 V in steps of 5 V. (e) Density of interface states and (f) trap response time as a function of gate bias. The fit values are determined by using equation 2-4. (g) Cole-Cole plot at gate bias of -25 V, 0 V, and 25 V (Arrows indicates increasing gate bias direction). Un-doped TFT: black. BV-doped TFT: red.

The equivalent circuit model in **Figure 2.9(a)** includes the parallel conductance G_p, the interface states capacitance C_{it}, and the depletion capacitance $C_{deplete}$ placed in parallel; the above components are in series with the gate dielectric capacitance C_g. The equivalent circuit as seen by the impedance analyzer is shown in **Figure 2.9(b)**, where the measured conductance G_m and measured capacitance C_m are in parallel. The parallel conductance and measured conductance are related[24] as follows

$$G_P = \frac{\omega^2 C_g{}^2 G_m}{G_m{}^2 + \omega^2 (C_g - C_m)^2} \tag{2-3}$$

Here C_g= 10 nF/cm^2 for the devices in this work and $\omega = 2\pi f$ is the angular frequency of the applied ac voltage. The measured capacitance is equivalent to $1/C_m = 1/C_g + 1/(C_{it} + C_{deplete})$. The real and imaginary components of admittance Y are described by the following expressions[24,25] derived from the Debye relaxation model:

$$\frac{Re(Y)}{\omega} = \frac{G_P}{\omega} = \frac{qD_{it}}{2\omega\tau} ln\left[1 + (\omega\tau)^2\right] \tag{2-4}$$

$$\frac{\mathrm{Im}(Y)}{\omega} = C_{it} + C_{deplete} = \frac{qD_{it}}{\omega\tau}\arctan(\omega\tau) + C_{deplete} \tag{2-5}$$

where D_{it} is the density of interface state and τ is the time constant for the capture and emission of trapped charges.

Figure 2.9(c), (d) compares the loss G_P/ω associated with charges moving into and out of interface states in un-doped and BV-doped TFTs. The peaks monotonically shift to higher frequencies with increasing gate bias, which indicates the presence of continuously distributed energy levels of interface traps. Maximum G_P/ω values at each gate bias is obtained to calculate the magnitude of D_{it}, and the fit values for τ are shown in **Figure 2.9(e), (f)**, respectively. The D_{it} for both devices increases with gate voltage, indicating higher density of interface states in the energy level close to conduction band. Likewise, charges spent shorter time τ in interface states with increasing gate bias. In comparison to un-doped TFTs, BV-doped devices show lower loss and higher peak frequency. There is lower density of interfacial trap states after BV treatment, showing the effectiveness of BV doping in removing interface states. Also, based on the observed time constants, faster capture and emission process are observed in the BV-doped devices as deep traps are reduced. The real and imaginary components of admittance Y are shown in **Figure 2.10**, where the oxide capacitance has been subtracted.

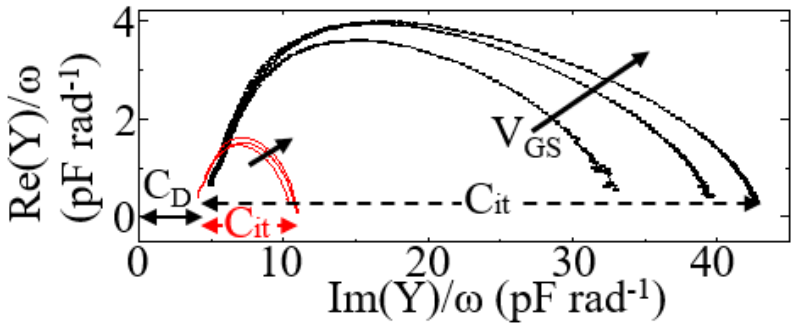

Figure 2.10. Cole-Cole plot at gate bias of -25 V, 0 V, and 25 V (Arrows indicates increasing gate bias direction). Un-doped TFT: black. BV-doped TFT: red.

This figure, also known as Cole-Cole plot,[26] provides additional graphical analysis without the need for fitting. The distance between the two intersection points with x-axis denotes the interface states capacitance $C_{it} = q D_{it} A$, where the area A is 0.183 mm by 1.13 mm here. The distance between the origin and x-intercept at high frequency indicates the depletion capacitance, which is around 4 pF for the devices here. At V_{GS}= 25 V, the C_{it} is estimated to be 38 pF for an un-doped TFT whereas it is 7.5 pF for a BV-doped TFT. These values are in good agreement with the expected capacitance calculated from the D_{it} in frequency-dependent G_P/ω plots.

2.5 Conclusions

The application of benzyl viologen on IZO surface achieved charge-transfer doping that increased the effective field-effect mobility, reduced contact resistance, and improved the stability of inkjet-printed IZO TFTs. The device mobility was enhanced and reached up to 8.7 ± 1.0 $cm^2(Vs)^{-1}$ after BV treatment. The analysis of frequency-dependent capacitance and admittance quantified the density of interface states, for which the BV-doped devices show four times lower trap density. In the future, to minimize the threshold voltage shift, the dopant concentration may be adjusted by changing the concentration of BV in the doping solution and the thickness of IZO layer. The air-stable, facile process of BV doping enables a new handle to improve printed IZO transistor performance.

Chapter 2, in part, are the reprint of the material as it appears in the publication: Hyonwoong Kim and Tse Nga Ng, "Reducing trap states in printed indium zinc oxide transistors by doping with benzyl viololgen", *Adv. Elec. Mater*., 1700631 (2018). The dissertation author was the primary author of the paper.

2.6 References

(1) Kamiya, T.; Hosono, H. Material Characteristics and Applications of Transparent Amorphous Oxide Semiconductors. *NPG Asia Mater.* **2010**, *2*, 15–22.

(2) Fortunato, E.; Barquinha, P.; Martins, R. Oxide Semiconductor Thin-Film Transistors: A Review of Recent Advances. *Adv. Mater.* **2012**, *24*, 2945–2986.

(3) Nadarajah, A.; Wu, M. Z. B.; Archila, K.; Kast, M. G.; Smith, A. M.; Chiang, T. H.; Keszler, D. A.; Wager, J. F.; Boettcher, S. W. Amorphous In-Ga-Zn Oxide Semiconducting Thin Films with High Mobility from Electrochemically Generated Aqueous Nanocluster Inks. *Chem. Mater.* **2015**, *27*, 5587–5596.

(4) Pecunia, V.; Banger, K.; Sirringhaus, H. High-Performance Solution-Processed Amorphous- Oxide-Semiconductor TFTs with Organic Polymeric Gate Dielectrics. *Adv. Electron. Mater.* **2015**, *1*, 1400024.

(5) Xu, X.; Feng, L.; He, S.; Jin, Y.; Guo, X. Solution-Processed Zinc Oxide Thin-Film Transistors with a Low-Temperature Polymer Passivation Layer. *IEEE Electron Device Lett.* **2012**, *33*, 1420–1422.

(6) Hennek, J. W.; Smith, J.; Yan, A.; Kim, M. G.; Zhao, W.; Dravid, V. P.; Facchetti, A.; Marks, T. J. Oxygen "Getter" Effects on Microstructure and Carrier Transport in Low Temperature Combustion-Processed a-InXZnO (X = Ga, Sc, Y, La) Transistors. *J. Am. Chem. Soc.* **2013**, *135*, 10729–10741.

(7) Park, S. Y.; Kim, B. J.; Kim, K.; Kang, M. S.; Lim, K. H.; Lee, T. Il; Myoung, J. M.; Baik, H. K.; Cho, J. H.; Kim, Y. S. Low-Temperature, Solution-Processed and Alkali Metal Doped Zno for High-Performance Thin-Film Transistors. *Adv. Mater.* **2012**, *24*, 834–838.

(8) He, Y.; Xia, F.; Shao, Z.; Zhao, J.; Jie, J. Surface Charge Transfer Doping of Monolayer Phosphorene via Molecular Adsorption. *J. Phys. Chem. Lett.* **2015**, *6*, 4701–4710.

(9) Kiriya, D.; Tosun, M.; Zhao, P.; Kang, J. S.; Javey, A. Air-Stable Surface Charge Transfer Doping of MoS2 by Benzyl Viologen. *J. Am. Chem. Soc.* **2014**, *136*,

7853–7856.

(10) Kim, S. M.; Jang, J. H.; Kim, K. K.; Park, H. K.; Bae, J. J.; Yu, W. J.; Lee, I. H.; Kim, G.; Loc, D. D.; Kim, U. J.; *et al.* Reduction-Controlled Viologen in Bisolvent as an Environmentally Stable n-Type Dopant for Carbon Nanotubes. *J. Am. Chem. Soc.* **2009**, *131*, 327–331.

(11) Lüssem, B.; Keum, C. M.; Kasemann, D.; Naab, B.; Bao, Z.; Leo, K. Doped Organic Transistors. *Chem. Rev.* **2016**, *116*, 13714–13751.

(12) Kwon, G.; Kim, K.; Choi, B. D.; Roh, J.; Lee, C.; Noh, Y. Y.; Seo, S. Y.; Kim, M. G.; Kim, C. Multifunctional Organic-Semiconductor Interfacial Layers for Solution-Processed Oxide-Semiconductor Thin-Film Transistor. *Adv. Mater.* **2017**, *29*, 1607055.

(13) Yu, S. H.; Kim, B. J.; Kang, M. S.; Kim, S. H.; Han, J. H.; Lee, J. Y.; Cho, J. H. In/Ga-Free, Inkjet-Printed Charge Transfer Doping for Solution-Processed ZnO. *ACS Appl. Mater. Interfaces* **2013**, *5*, 9765–9769.

(14) Ng, T. N.; Schwartz, D. E.; Mei, P.; Krusor, B.; Kor, S.; Veres, J.; Broms, P.; Eriksson, T.; Wang, Y.; Hagel, O.; *et al.* Printed Dose-Recording Tag Based on Organic Complementary Circuits and Ferroelectric Memories. *Sci. Rep.* **2015**, *5*, 13457.

(15) Ng, T. N.; Schwartz, D. E.; Mei, P.; Kor, S.; Veres, J.; Bröms, P.; Karlsson, C. Pulsed Voltage Multiplier Based on Printed Organic Devices. *Flex. Print. Electron.* **2016**, *1*, 015002.

(16) Mashayekhi, M.; Conde, A.; Ng, T. N.; Mei, P.; Ramon, E.; Martinez-Domingo, C.; Alcalde, A.; Teres, L.; Bordoll, J. C. Inkjet Printing Design Rules Formalization and Improvement. *IEEE/OSA J. Disp. Technol.* **2015**, *11*, 658–665.

(17) Street, R. A.; Ng, T. N.; Lujan, R. A.; Son, I.; Smith, M.; Kim, S.; Lee, T.; Moon, Y.; Cho, S. Sol-Gel Solution-Deposited InGaZnO Thin Film Transistors. *ACS Appl. Mater. Interfaces* **2014**, *6*, 4428–4437.

(18) Secor, E. B.; Smith, J.; Marks, T. J.; Hersam, M. C. High-Performance Inkjet-Printed Indium-Gallium-Zinc-Oxide Transistors Enabled by Embedded,

Chemically Stable Graphene Electrodes. *ACS Appl. Mater. Interfaces* **2016**, *8*, 17428–17434.

(19) Miyadera, T.; Minari, T.; Tsukagoshi, K.; Ito, H.; Aoyagi, Y. Frequency Response Analysis of Pentacene Thin-Film Transistors with Low Impedance Contact by Interface Molecular Doping. *Appl. Phys. Lett.* **2007**, *91*, 013512.

(20) Lee, S.; Ghaffarzadeh, K.; Nathan, A.; Robertson, J.; Jeon, S.; Kim, C.; Song, I.-H.; Chung, U.-I. Trap-Limited and Percolation Conduction Mechanisms in Amorphous Oxide Semiconductor Thin Film Transistors. *Appl. Phys. Lett.* **2011**, *98*, 203508.

(21) Ng, T. N.; Chabinyc, M. L.; Street, R. A.; Salleo, A. Bias Stress Effects in Organic Thin Film Transistors. In *IEEE International Reliability Physics Symposium*; Phoenix, 2007; pp. 243–247.

(22) Lee, W. H.; Choi, H. H.; Kim, D. H.; Cho, K. 25th Anniversary Article: Microstructure Dependent Bias Stability of Organic Transistors. *Adv. Mater.* **2014**, *26*, 1660–1680.

(23) Torres, I.; Taylor, D. M. Interface States in Polymer Metal-Insulator-Semiconductor Devices. *J. Appl. Phys.* **2005**, *98*.

(24) Engel-Herbert, R.; Hwang, Y.; Stemmer, S. Comparison of Methods to Quantify Interface Trap Densities at Dielectric/III-V Semiconductor Interfaces. *J. Appl. Phys.* **2010**, *108*, 124101.

(25) Siddiqui, J. J.; Phillips, J. D.; Leedy, K.; Bayraktaroglu, B. Admittance Spectroscopy of Interface States in ZnO / HfO_2 Thin-Film Electronics. *IEEE Electron Device Lett.* **2011**, *32*, 1713–1715.

(26) Malmin, P. C. Cole-Cole Plotting of Surface State Admittance in MIS Capacitors. *Phys. Status Solidi* **1971**, *8*, 597–603.

Chapter 3 Application of Indium Zinc Oxide Thin Film Transistors in Phototransistors

3.1 Abstract

This report demonstrates high-performance infrared phototransistors that uses a broadband absorbing organic bulk heterojunction (BHJ) layer responsive from the visible to the shortwave infrared, from 500 nm to 1400 nm. The device structure is based on a bilayer transistor channel that decouples charge photogeneration and transport, enabling independent optimization of each process. The organic BHJ layer is improved by incorporating camphor, a highly polarizable additive that increases carrier lifetime. An indium zinc oxide transport layer with high electron mobility is employed for rapid charge transport. As a result, the phototransistors achieve a dynamic range of 127 dB and reach a specific detectivity of 5×10^{12} Jones under low power illumination of 20 nW/cm^2, outperforming commercial germanium photodiodes in the spectral range below 1300 nm. The photodetector metrics are measured with respect to the applied voltage, incident light power, and temporal bandwidth, demonstrating operation at video-frame rate of 50 Hz. In particular, the frequency and light dependence of the phototransistor characteristics are analyzed to understand the change in photoconductive gain under different working conditions.

3.2 Introduction

3.2.1 Figure of Merit of Photodetectors

As the starting point of understanding SWIR OPD performance, some important characterization metrics are to be introduced in this section. A basic figure of merit that quantifies the strength of photo-response is the responsivity (R), which measures the electrical output per optical input. What is closely related to R is external quantum efficiency (EQE), which quantifies the conversion efficiency of incident photons to charge carriers. Another important quantity is noise spectral density (S_n), which represents the electrical signal generated in the absence of light. The overall figure of merit for photodetection, specific detectivity (D^*), corresponds to the signal-to-noise ratio (SNR) setting the detection bandwidth to 1Hz and the device area to 1 cm^2 at an incident power of 1W. These important metrics are summarized in

Table 3.1 and will appear throughout the rest of the dissertation. In addition to these metrics, some other figures of merit are also commonly characterized in photodetector works, such as the linear dynamic range (LDR) (measures the range of incident light power over which the detector response is linear), -3dB bandwidth (characterizes the temporal response and is limited by carrier transit time (t_{tr}) , RC time or both) and noise equivalent power (NEP) (indicates the incident power that would be required to yield a near-unity SNR over a bandwidth of 1Hz. D^* normalizes the NEP to the device area and detection bandwidth).

Table 3.1. Definitions of photosensor metrics.

Metric	Definition
External quantum efficiency (EQE)	The ratio between the number of collected carriers and incident photons: $EQE = R\frac{hc}{\lambda q}$, where $R = \frac{J_{ph}}{P_{light}}$ is the responsivity, J_{ph} is the photocurrent density, P_{light} is the intensity of the incident light per unit area, h is Planck's constant, c is the speed of light, λ is the wavelength of light, and q is the elementary charge. EQE is unitless and often expressed as a percentage.
Noise spectral density (S_n)	The noise spectral density origins from multiple noise sources, including shot noise, thermal noise and 1/f (flicker) noise. The total noise spectral density is expressed as $S_n = \sqrt{{S_{shot}}^2 + {S_{thermal}}^2 + {S_{\frac{1}{f}}}^2}$. Shot noise is related to the current by $S_{shot} = \sqrt{2qI}$, where q is the elementary charge and I is the current flowing through the device. Thermal noise is given by $S_{thermal} = \sqrt{4kT/R_{sh}}$, where k is Boltzman's constant, T is the temperature, and R_{sh} is the shunt resistance of the device. 1/f noise is empirical and usually not expressed in terms of device parameters. The unit of S_n is A/√Hz.
Specific detectivity (D^*)	The signal-to-noise ratio of responsivity to dark noise: $D^* = \frac{R\sqrt{A}}{S_n}$, where R is the responsivity, A is the effective device area, and S_n is the noise spectral density. The unit of D^* is Jones (1 Jones = 1 cm √Hz /W).

3.2.2 Photodiode versus Phototransistors

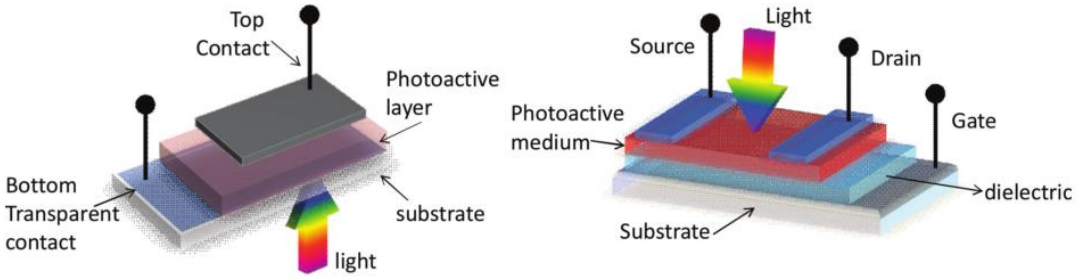

Figure 3.1. Schematic illustration of typical device structure of (left) photodiode and (right) phototransistor[1].

Representative photodetectors can be divided into phototdiodes and phototransistors. In terms of device structure, photodiodes and phototransistors are not different from typical p-n diodes and transistors as shown in **Figure 3.1.** The most distinct difference between photodiodes and phototransistors are presence of photoconductive gain in phototransistor. Comparison of photodiodes and phototransistors are shown in **Table 3.2**.

Table 3.2. Comparison of typical behaviors of photodiodes and phototransistors

Metric	Photodiodes	Phototransistors
An incident photon	Generates single electron-hole pair at best	Induces one type of carrier recirculation
EQE	< 100%	Can exceed 100%
Response time	Fast (~ns to μs)	Slow (~ms)
LDR	Relatively low (Linear)	Wide (Sublinear)

In photodiodes, when excitons are generated under illumination, excitons are dissociated into electrons and holes, eventually free carriers are collected by anode and cathode, respectively. Therefore, single incident photon generates single electron-hole pair at best. However, as shown in **Figure 3.2**, in phototransistors, one type of (either electron or hole) free carriers are trapped in semiconductor, meanwhile another type of carrier is collected by source/drain electrodes. In order to maintain the charge neutrality in semiconductor, free carriers are continuously injected and extracted. This leads to the recirculation of one type of carrier, resulting in photoconductive gain, which is an exclusive behavior of phototransistor. Therefore, single photon enables collection of multiple of free carrier (either electrons or holes), resulting in EQE over 100% and photo-signal amplification. In terms of photosignal amplification, phototransistor is advantageous over photodiode. However, photodiodes exhibit faster response than that of phototransistors. Due to the photoconductive gain in phototransistors, there is still current in the dark ambient for a carrier lifetime of trapped carriers.

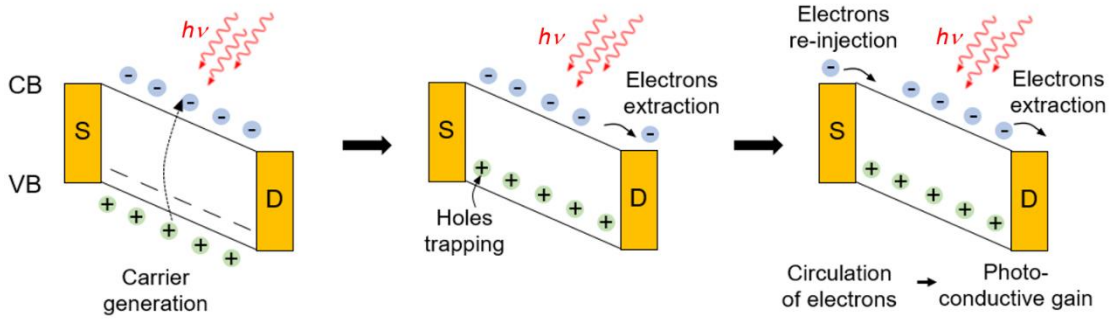

Figure 3.2. Schematic illustration of photoconductive gain mechanism in phototransistors under illumination of n-type semiconductor with trapped holes.

3.2.3 Application of Infrared Light

Infrared light (IR) provides another window to see beyond visible range. As shown in **Figure 3.3**, IR enables vision through smoke and haze. Recently, people become more interested in the spectrum beyond near infrared light (NIR, 0.7 μm <λ< 1.1 μm), which is called as shortwave infrared (SWIR) light. Since SWIR (1.1 μm <λ< 3 μm) has deeper penetration depth as shown in **Figure 3.4**, there has been increasing study on employing SWIR light for bio-signal detection. **Figure 3.5** shows images of mouse skull by using different light spectrum. Due to the higher contrast, less light scattering, and deeper penetration depth, images taken by SWIR light detection shows the highest resolution.

Figure 3.3. SWIR detection enables imaging through smoke and haze. (sensorisinc.com)

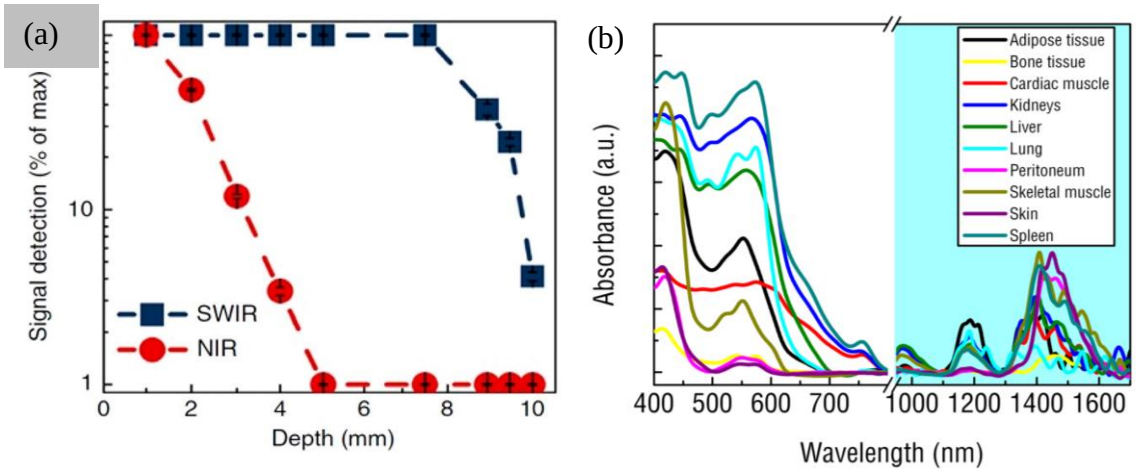

Figure 3.4. (a) Comparison of penetration depth between NIR and SWIR detection. NIR light shows complete attenuation by 5 mm, whereas SWIR light can be detected through 10 mm of phantom tissues.[2] (b) Light absorbance versus spectral wavelength through various tissue samples.[2]

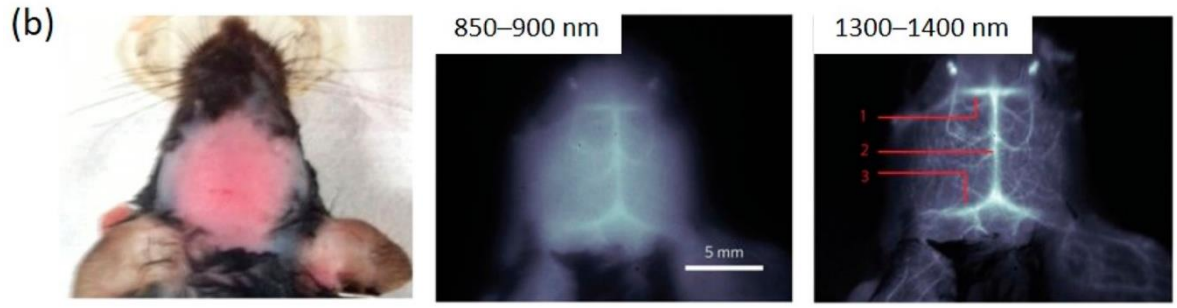

Figure 3.5. *In vivo* mouse brain fluorescence imaging in different spectral regions.[3]

Based on the advantages of SWIR light, Zhenghui et al., achieves SWIR photodiodes array by using back-to-back diode as a pixel. In their research, their array distinguishes lean meat and fat depending on the difference in transmittance as shown in **Figure 3.6.**

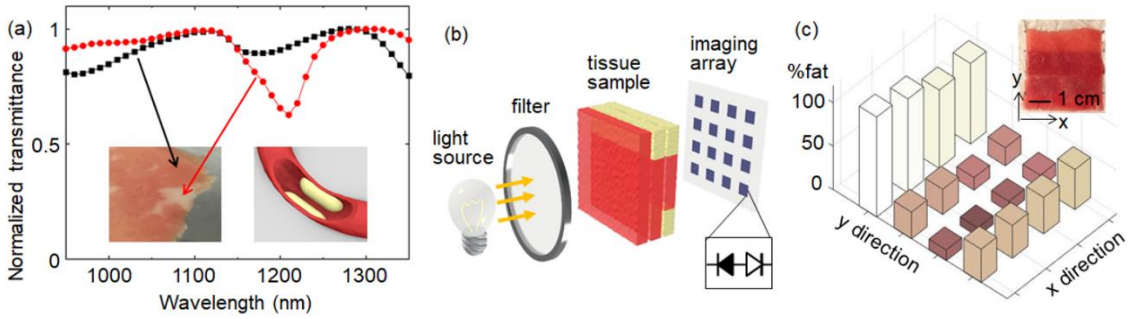

Figure 3.6. (a) Normalized transmittance spectra of muscular (black) and fatty tissues (red). The inset schematic shows the scenario of fatty deposits clogging an artery. (b) Measurement setup for SWIR spectral imaging. The image of tissue sample is portrayed according to actual arrangement of muscular and fatty layers. (c) Percentage of fatty tissues at each pixel location. The inset photograph shows the actual sample for imaging.[4]

3.2.4 Decoupling of Light Absorption and Carrier Transport

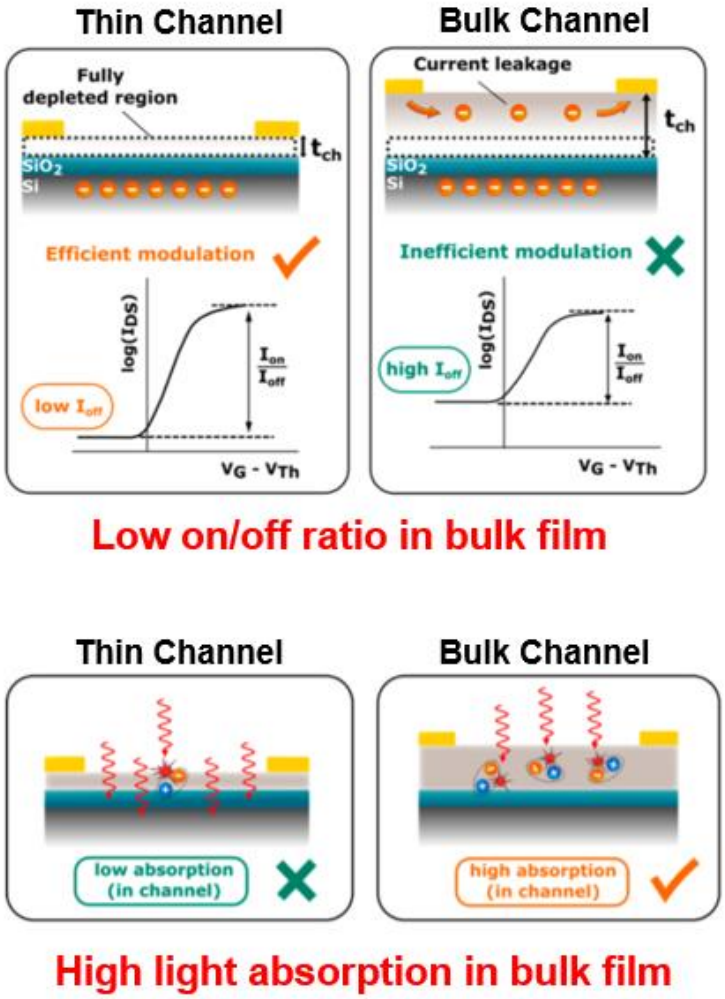

Figure 3.7. Inherent limitation in single semiconductor-equipped phototransistor. Trade-off between on/off current ratio and absorption occurs. (a) Inferior on/off current ratio in phototransistor with bulk film active layer. (b) superior absorption in the phototransistor with bulk film active layer.[5]

Typical phototransistors have mainly utilized single semiconductor as active layer, that absorbs the light of interest and transports carrier. However, phototransistors with

single semiconductor have inherent limitation. In case of phototransistor using bulk active semiconductor film, it absorbs more photons but on/off current ratio is deteriorated simultaneously. In photodetectors, on/off ratio is an important parameter that affects signal-to-noise ratio. In case of using thin active layer to improve on/off current ratio, there is accompanying issue in low light absorption. In order to circumvent inherent trade-off in phototransistor with single semiconductor, bilayer structure have been proposed. In phototransistors with bilayer structure, it decouples light absorption and carrier transport, enabling individual optimization of each layer in more efficient way.

Organic semiconductors offer highly tunable optoelectronic properties and the advantages of economical large-area deposition and low-temperature processing. In particular, solution-processed semiconducting polymers are being developed which extend the spectral range of these materials beyond the visible, to enable scalable large-area photodetectors responsive to near- (NIR: 0.75–1 μm) and shortwave infrared (NIR: 1–3 μm) radiation.[6–8] As the bandgap of the materials are further reduced for infrared detection,[4,9,10] the device performance becomes increasingly restricted by non-radiative recombination[11–13] of photogenerated carriers. Charge recombination may occur during the exciton dissociation step or during charge transport, and optimization of each step is desirable but is complicated in bulk heterojunction (BHJ) architectures. In BHJ photodiodes, a large interfacial area between the donor and acceptor components facilitates exciton dissociation into free carriers, which must then navigate

interpenetrating donor and acceptor phase-separated domains to reach their respective electrodes. The nature of the interfaces, structural and energetic heterogeneities, and disordered domains impede carrier transport within these systems. As such, it has been challenging to address the conflicting requirements in a single active layer.[1,14,15] As an alternative, bilayer phototransistor structures[16–21] are being designed to decouple both materials and processes associated with charge photogeneration and transport to improve device performance.

Phototransistors use the applied electric field from the gate electrode to promote photoconductive gain. The gain mechanism[22–25] originates from trap states within the semiconductor bandgap. After photogeneration of electron-hole pairs, one carrier type is captured and localized in the traps. The opposite carrier type is collected and also injected under bias between the source and drain electrodes to maintain charge neutrality in the semiconductor channel. Within the trapped carrier lifetime, injected carriers circulate multiple times, leading to amplification of the photocurrent and external quantum efficiency (EQE) exceeding 100%. The photoconductive gain is proportional to the ratio of $\tau_{trap}/\tau_{transit}$, where τ_{trap} is the trapped carrier lifetime and $\tau_{transit}$ is the transit time across the transistor channel. Thus extending the carrier lifetime and reducing transit time are needed to increase gain.

The phototransistor structures here address the recombination issue and enhance photoconductive gain by using separate layers for charge photogeneration and transport.

The photogeneration materials are chosen to be responsive to infrared wavelengths (λ) out to 1400 nm. Since the probability of recombination increases in narrow bandgap IR materials, the organic BHJ layer is tuned with a high-permittivity molecule camphor,[26,27] to assess whether the polarizable additive would stabilize photogenerated charge and improve carrier lifetimes. In our system, the photogenerated holes are trapped in the BHJ, while electrons circulate in the transport layer consisting of inkjet printed indium zinc oxide (IZO),[28,29] which offers a higher mobility than organic materials and the potential for low-cost, large-area integration in pixelated imagers.[16,30] The key photodetector characteristics, including temporal bandwidth, detectivity, photoconductive gain, and dynamic range, are analyzed for two compositions at various operational voltages and bandwidths. To ensure correct characterization, we pay attention to the frequency and light dependence of the phototransistor characteristics, in order to understand the change in photoconductive gain under different working conditions. This novel IR phototransistor design is shown to exceed the performance of commercial germanium photodiodes at video rate spanning the visible to the shortwave IR ($500 < \lambda < 1300$ nm) under low light illumination.

3.3 Experimental Procedures

3.3.1 Phototransistor Fabrication

A heavily p-doped Si wafer with 300 nm thermal oxide was UV-ozone treated for 5 min to remove organic residue and enhance the wettability. The IZO ink was consisted of 0.12 M of indium nitrate hydrate and 0.08 M of zinc nitrate hexahydrate in 2-methoxyethanol.[28,29] The IZO precursor solution was printed using inkjet[31,32] (Fujifilm Dimatix DMP2800), with the substrate heated at 60°C. The printed IZO film was annealed at 400°C in air for 2 hr. For contact electrodes, 40 nm aluminum was thermally deposited in ~2×10^{6} mbar vacuum. Aluminum was used to match the work function for electron injection/extraction and reducing hole injection/extraction. The transistor channel dimension was 30 μm length ×1000 μm width. The BHJ solution was prepared by mixing 1 mg/mL of donor polymer and 2 mg/mL of $PC_{71}BM$ (>99%, Ossila) in toluene with 3 vol% of diiodooctane (98%, Sigma Aldrich). The synthesis procedure for the donor polymer is found in Supplement and in reference [26]. For films with 1,7,7-trimethylbicyclo[2.2.1]heptan-2-one (±)-camphor (Sigma Aldrich), the desired weight percentage is added to the BHJ solution. Prior to BHJ deposition, the IZO TFT was annealed at 120°C in nitrogen to desorb water molecules. The BHJ solution was spin coated at 5000 rpm for 60 s and vacuum dried for 10 min. For encapsulation, device was sealed with a glass slide bonded with epoxy.

3.3.2. Device Characterization

In the EQE measurements,[33] the monochromatic light source was modulated at 10 Hz by an optical chopper, and the device photocurrent was amplified through a low-

noise amplifier (SR570, Stanford Research Systems) and measured with a lock-in amplifier (SRS530, Stanford Research Systems). Filters with cut-off wavelengths of 455, 645, 1025 nm were used to reduce the scattered light from higher order diffraction. The incident light power is measured with a Ge photodiode (818-IR, Newport Corporation) for 780-1400 nm range, a Si photodiode (DET36A, Thorlabs) for 460-780 nm. Electrochemical impedance spectroscopy was performed with a potentiostat (SP200, Bio-logic) over the frequency range of 100 Hz to 2 MHz with 100 mV amplitude, with the phototransistor gate electrode floating.

A lock-in amplifier was used to measure the noise current density. The background noise current external to the device (i.e., preamplifier, leads, etc.) contributed to the total noise current and was measured by connecting the leads with no device in place. The device was connected to the preamplifier at the source and drain electrodes, while external bias voltages were applied to the gate (V_{GS}= 0 V or -10 V) and drain electrodes (V_{DS}= 5 V). The background noise was subtracted from the total noise to obtain the device noise. Preamplifier was in low-noise mode, and the noise current density was an average from 10 measurements at each frequency.

To measure the temporal response of phototransistors, a light emitting diode (LED) with center wavelength of 940 nm and spectral width of 50 nm was used as the light source. Light power was tuned by placing neutral density filters over the device. The input voltage waveform to the LED was controlled by a function generator. The transistor

photocurrent is converted to voltage through a preamplifier in high bandwidth mode, and the output voltage is recorded by an oscilloscope.

3.4 Results and Discussions

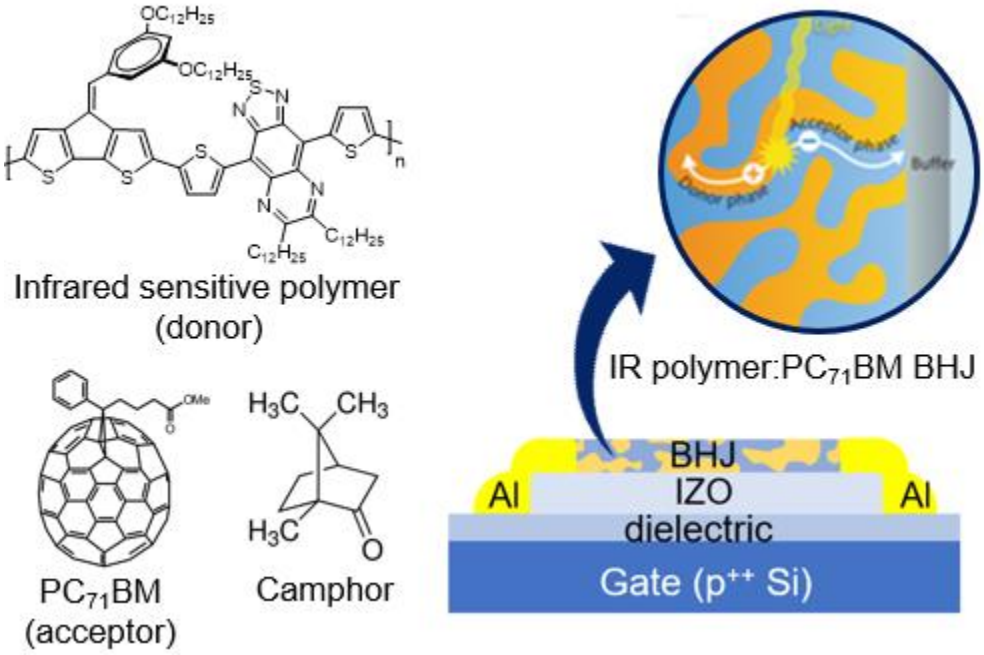

Figure 3.8. (a) Chemical structures of materials in the bulk heterojunction (BHJ) layer. (b) Bilayer phototransistor structure with indium zinc oxide (IZO) as the electron transporting layer and BHJ as light absorption layer.

Figure 3.8(a) shows the chemical structures of the materials in the BHJ layer, which includes a blend of a narrow bandgap IR absorbing polymer[26] as the donor, [6,6]-Phenyl-C71-butyric acid methyl ester ($PC_{71}BM$) as the acceptor. The donor-to-acceptor ratio is 1:2 by weight, and devices are fabricated with or without camphor as the high-

permittivity additive. For films with camphor (1,7,7-trimethylbicyclo[2.2.1]heptan-2-one (±)-camphor), the weight percentage of the additive is 23%, which is the maximum that can be added without crystallite formation.[27] **Figure 3.8(b)** illustrates the phototransistor structure in a bottom-gate, top-contact configuration. The effective mobility of IZO transistors before BHJ deposition is measured to be 0.83 ± 0.07 cm^2/Vs at saturation, as shown in **Figure 3.9**.

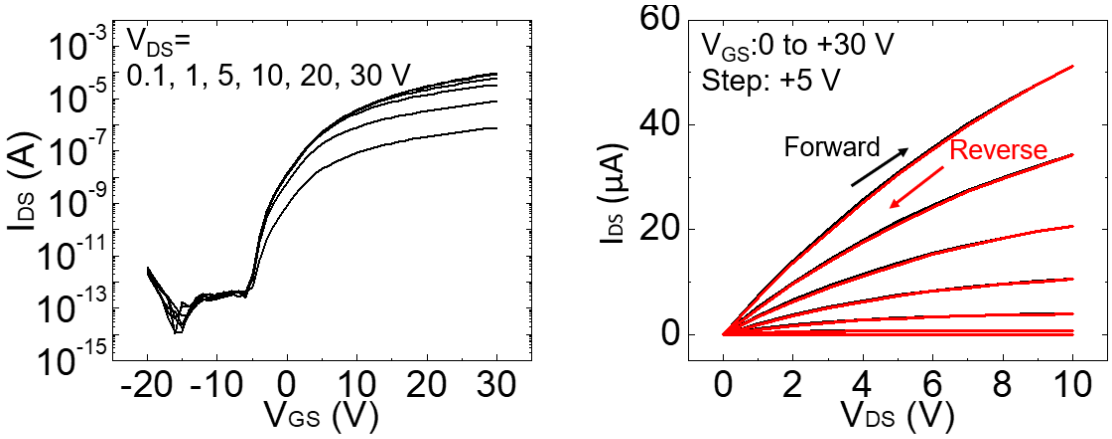

V_{th} [V]	V_{on} [V]	S.S [V/dec]	$I_{on/off}$	μ_{sat} [$cm^2/V \cdot s$]
2.84±0.26	-6.42±1.74	0.62±0.02	~10^8	0.83±0.07

Figure 3.9. Representative current-voltage characteristics of indium zinc oxide (IZO) transistors in the dark, showing negligible hysteresis. The statistics on 15 IZO transistors are shown in the table.

The absorption spectra of BHJ materials show no significant spectral shift upon camphor addition. The BHJ absorption spectra and electrochemical measurements used to determine the polymer energy levels are included in **Figure 3.10**. **Figure 3.10(a)** shows the normalized absorption spectra of pure infrared (IR)-sensitive polymer, PC71BM, and

bulk heterojunction (BHJ) films with and without camphor. IR-sensitive polymer with narrow band gap enables light absorption up to 1400 nm with the peak absorbance at ~1100 nm. Absorbance of BHJ film is in good agreement as the summation of individual absorbances of IR polymer and $PC_{71}BM$. Absorbances of two BHJ films with and without camphor show identical absorption spectrum.

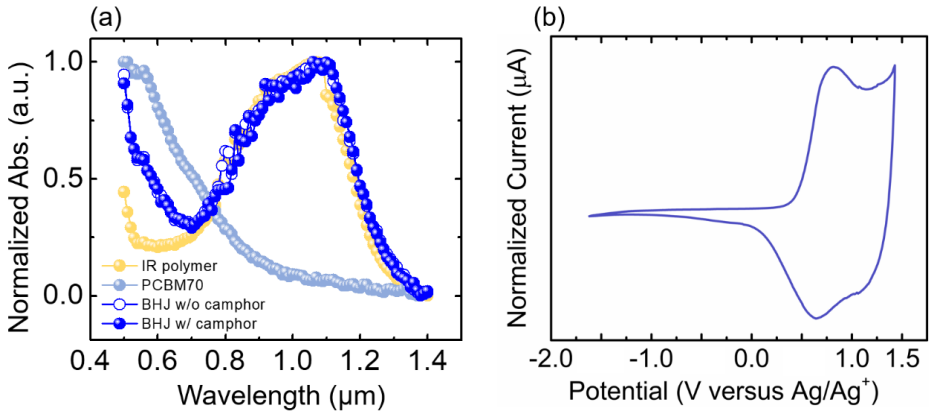

Figure 3.10. (a) Normalized absorption spectra of IR-sensitive polymer, $PC_{71}BM$, bulk heterojunction (BHJ) film with and without camphor. (b) Cyclic voltammetry of IR-sensitive polymer. The lowest unoccupied molecular orbital (LUMO) is estimated to be -3.65 eV, and the highest occupied molecular orbital (HOMO) is -4.75 eV.

The energy band diagram for the combination of a BHJ layer on top of an IZO transport channel is depicted in **Figure 3.11.** Under illumination, incident photons generate excitons, which are dissociated into electrons and holes at donor-acceptor interfaces in the BHJ. Due to the energy barrier for holes, holes are trapped[17,34] in the BHJ while electrons are spontaneously transferred to the IZO channel. As a result,

electrons circulate multiple times to maintain charge neutrality until the holes recombine, inducing photoconductive gain.

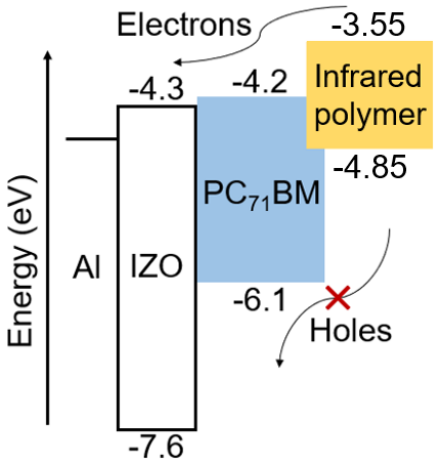

Figure 3.11. Energy diagram illustrating electrons transfer from the BHJ to IZO, whereas holes are trapped in BHJ.

IZO is a wide bandgap materials that does not show photoresponse in the IR, and the organic BHJ is responsible for infrared photogeneration as shown in **Figure 3.12**.

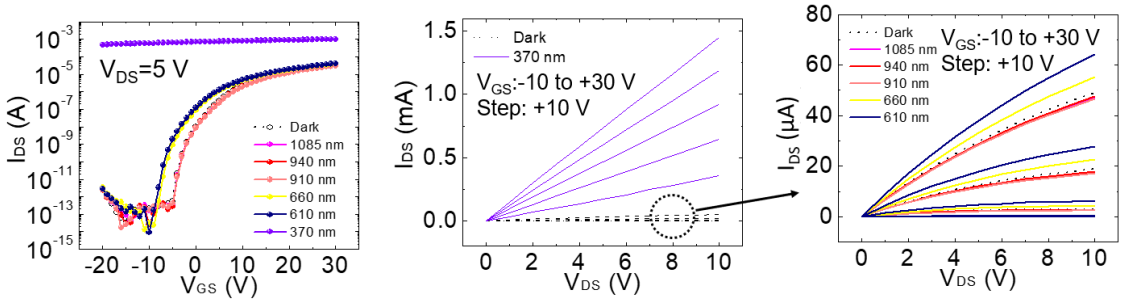

Figure 3.12. Current-voltage characteristics of an IZO transistor under LED light at different wavelength. Incident light with wavelength shorter than 660 nm leads to current increase and negative shift of V_{on} due to the sub-gap states in printed IZO. For bare IZO transistors without organic BHJ, the current remains unchanged under light in the infrared region.

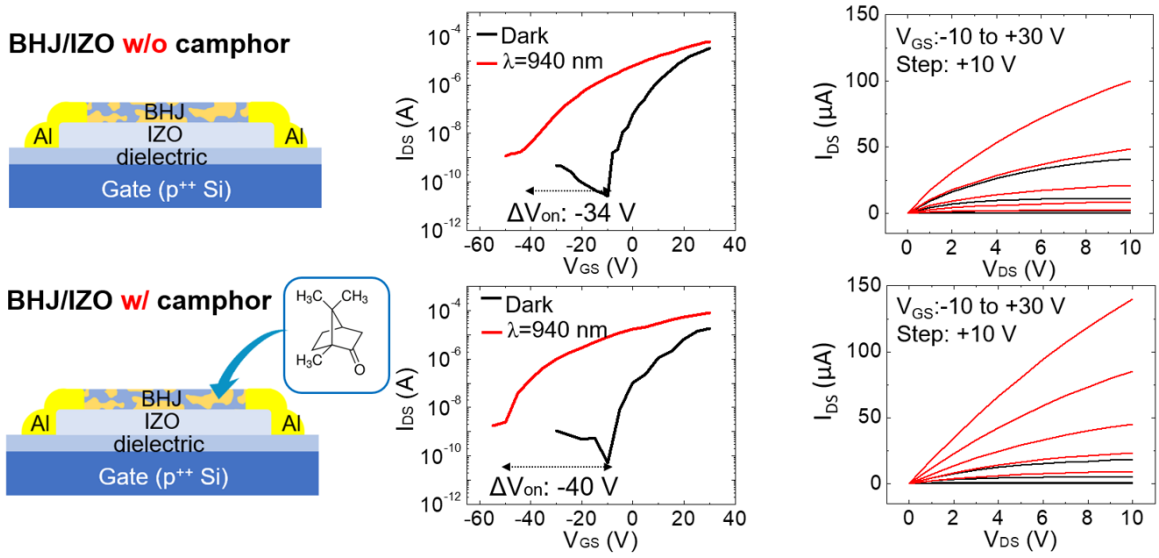

Figure 3.13. Current-voltage characteristics of phototransistors (top) without camphor and (bottom) with camphor. Transfer characteristics are measured at V_{DS} =5 V. Red: under light illumination. Black: dark ambient. The light was from a LED emitting at 940 nm wavelength with a power of 50 mW/cm^2.

Figure 3.13 shows the current-voltage characteristics of the BHJ-IZO phototransistors. With or without camphor, the BHJ-IZO devices show a similar turn-on voltage V_{on}= -10 V in the dark. Under λ = 940 nm irradation of 50 mW/cm^2, the V_{on} shifts in the negative direction due to trapped holes, changing by 40 V for the device with camphor and by 34 V for the one without camphor. The photocurrent, which is $I_{ph} = I_{light} - I_{dark}$, is higher for the device with camphor across all gate voltages.

The phototransistor output characteristics and comparisons to alternative device structures, such as a single layer BHJ without IZO, or a planar junction instead of BHJ, are included in **Figure 3.14**.

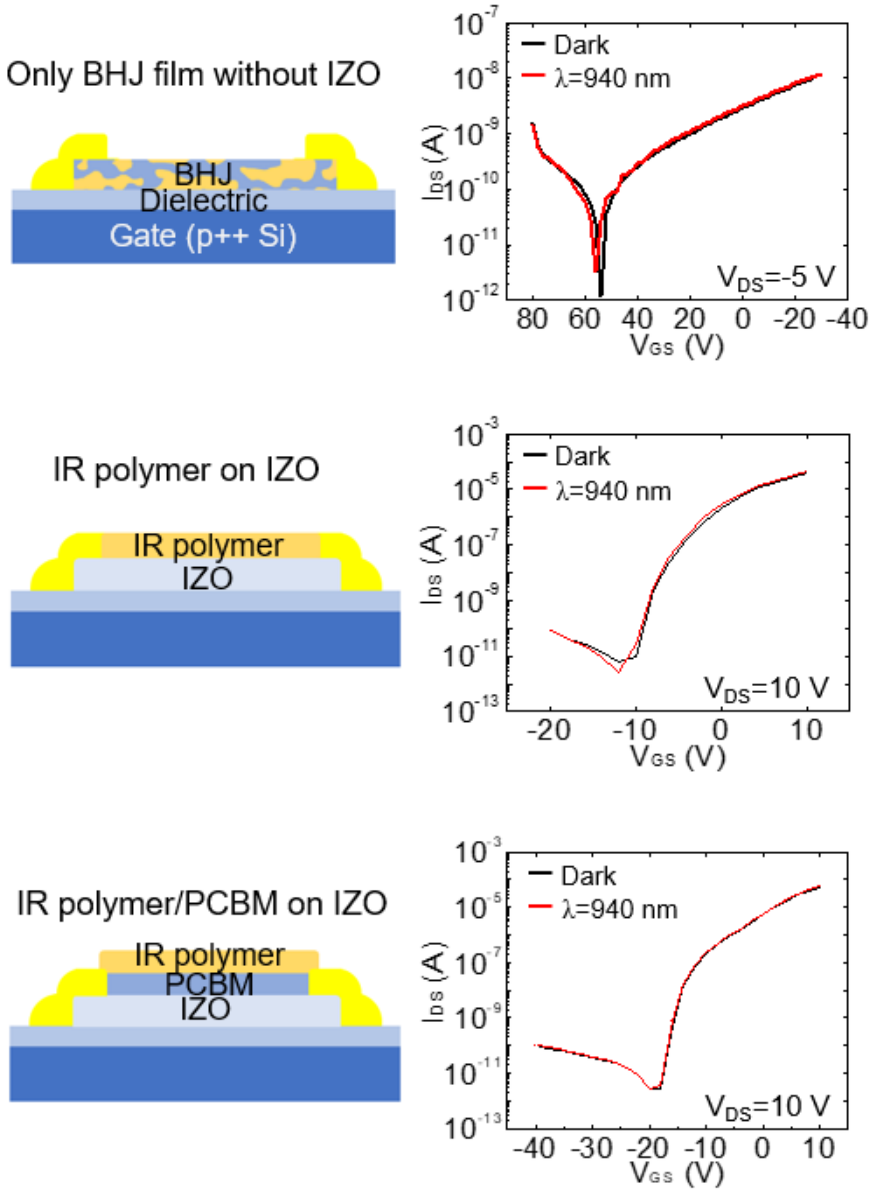

Figure 3.14. Current-voltage characteristics of alternative device structures under 940 nm IR light.

Figure 3.14 shows three different phototransistor structures. In the BHJ transistors without IZO (top in **Figure 3.14**), light absorption and carrier transport take place in the same place. In this structure, carrier transport is impeded by non-continuous path and the low mobility of IR-sensitive polymer and $PC_{71}BM$. When a planar junction of IR polymer/PCBM (middle in **Figure 3.14**) and IR polymer (bottom in **Figure 3.14**) are placed on IZO, the interfacial area in the planar junction is significantly smaller than in the BHJ. With smaller interfacial area, only excitons generated within the ~10 nm exciton diffusion length are dissociated into free carriers in planar junction. The photoresponse is poor in structures **Figure 3.14.**

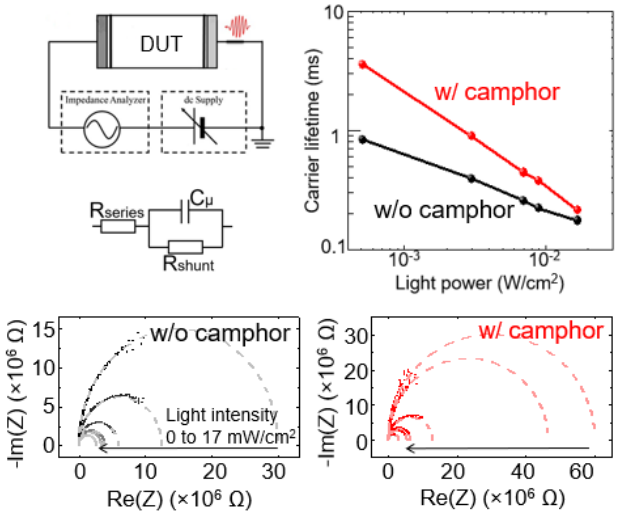

Figure 3.15. (a) Schematic diagram of electrochemical impedance spectroscopy measurement system and equivalent circuit. (b) Carrier lifetime versus incident light power. Nyquist plots of phototransistors in which the BHJ is (c) without camphor (black) versus (d) with camphor (red). Measurements were taken in the dark and under light power of 0.5, 3, 7, 9, and 17 mW/cm^2. Arrows point in the direction of increasing light intensity. Dashed lines indicate fits to the equivalent circuit shown in the inset of (a).

To investigate how the camphor additive increases photocurrent, the phototransistors are analyzed through electrochemical impedance spectroscopy under different illumination power as shown in **Figure 3.15(a)**. The source and drain electrons are connected to the potentiostat while a sinusoidal waveform with a 100 mV amplitude is applied over a frequency range of 100 Hz to 2 MHz. The Nyquist plots are fitted to an equivalent circuit[35] with components of shunt resistance R_{shunt} and capacitance C in parallel, which are in series with series resistance R_{series}. The fit values of R_{shunt}*C are estimates of the carrier lifetime, displayed in **Figure 3.15(b)**. These measurements cannot differentiate between electrons and holes and report their average lifetime before recombination. The carrier lifetime is consistently longer in the BHJ with camphor than in the film without camphor, in agreement with prior work[26,36] that high-permittivity environment can stabilize free carriers.

3.4.1. Characteristics with Respect to Sampling Frequencies

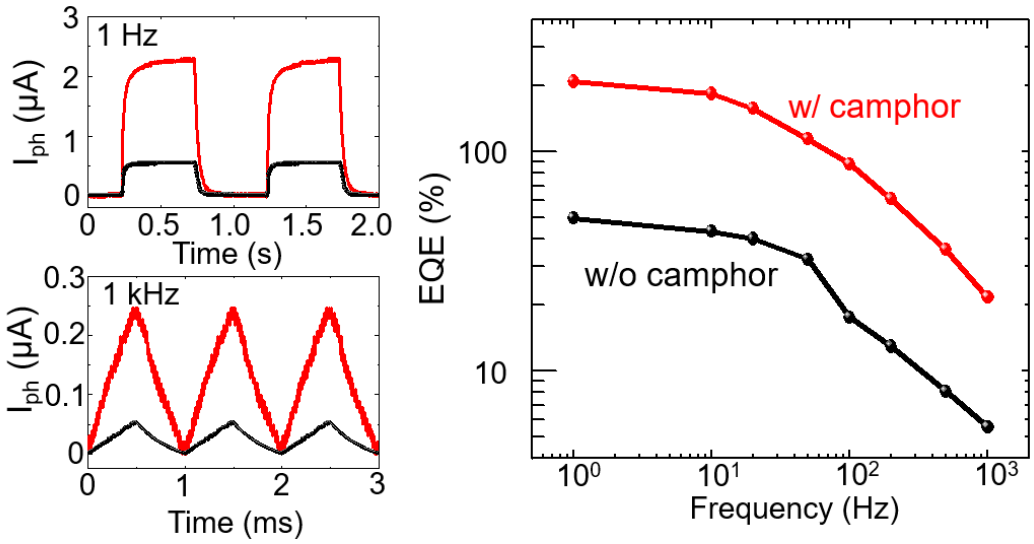

Figure 3.16. Photocurrent versus time, as the incident light is switched on and off at frequencies of (a) 1 Hz and (b) 1 kHz. (c) External quantum efficiency versus temporal bandwidth. Parts (a—c) are measured at V_{GS}= -10V and V_{DS} =5 V, under a light power of 5 mW/cm^2 at 940 nm wavelength.

The photocurrent in **Figure 3.16(a), (b)** shows the effects of photoconductive gain with time, as incident light pulses are modulated at different temporal frequencies. When the light source is switched on and off at 1 kHz, the photocurrent shows a monotonic rise and fall, and does not settle to a constant value because the circulation of injected electrons enables a gain in the photocurrent over time. At a slow frequency of 1 Hz, the photocurrent reaches a plateau, and the maximum gain is dictated by the equilibrium between the circulation time of injected electrons and the de-trapping time of

photogenerated holes. It is worth noting that the photocurrent rise/decay time in temporal response is different by an order of magnitude from the carrier lifetime obtained from the Nyquist plots. Carrier lifetime only reflects the time taken for excess carrier recombination via band-to-band or trap-assisted recombination. In devices with photoconductive gain, the photocurrent decay time is determined by the de-trapping time of the trapped carriers that is at a longer time scale than recombination.[25,37] While a long τ_{trap} can result in persistent photoconductivity and limits the refresh rate, switching the gate bias to recombine the trapped charges[30] can improve the refresh rate.

The external quantum efficiency (EQE) increases with lower light modulation frequency as seen in **Figure 3.16(c).** The EQE is calculated from the equation $EQE = (I_{ph}*h*c)/(q*P_{inc}*\lambda) = R(h*c)/(q*\lambda)$, where h is Planck's constant, c is the speed of light, q is charge, P_{inc} is the incident light power, λ is the incident light wavelength, and $R= I_{ph}/P_{inc}$ is the responsivity in unit of ampere per watt. The photocurrent I_{ph} is the value at the end of an illumination cycle. The EQE starts to decrease around 50 Hz, as there is less time for electrons to recirculate and amplify the photocurrent through photoconductive gain. Nonetheless, the roll-off frequency of 50 Hz allows video-rate recording.

3.4.2. Characteristics with Respect to Applied Voltages

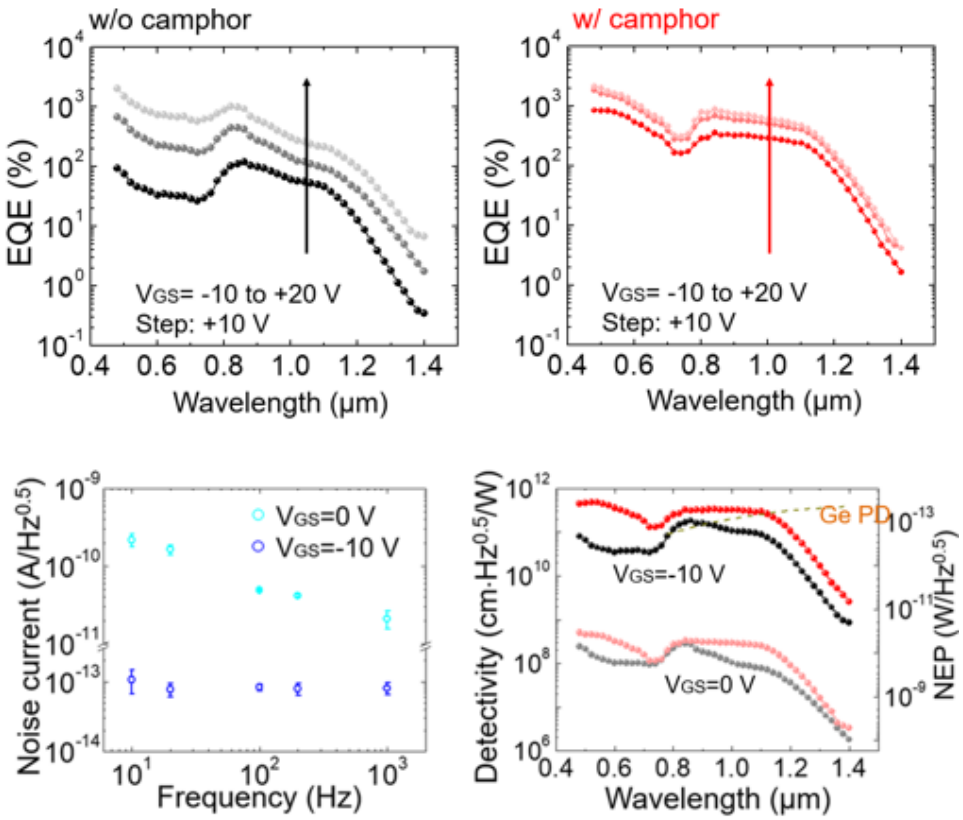

Figure 3.17. External quantum efficiency versus incident light wavelength, for phototransistors (a) without and (b) without camphor and operating under different gate bias conditions. (c) Noise current in the dark under different gate bias conditions versus frequency. (d) Detectivity and noise equivalent power of the phototransistors versus incident light wavelength. The source-drain bias is fixed at 5 V and the incident light is 0.3-0.5 mW/cm^2, modulated at a frequency of 10 Hz. The dashed line indicates the performance of a commercial germanium photodiode (818-IR, Newport Corporation).

In addition to dependence on the operational frequency, the photocurrent and EQE are dependent on the applied gate bias V_{GS}. As the phototransistor gate bias switches the channel from the depletion to the accumulation regime, the EQE increases up to ~1000%

as shown in **Figure 3.17(a), (b)**. In the accumulation regime, the positive gate bias attracts electrons to the IZO channel, resulting in a high effective mobility and raising photocurrent. In the depletion regime, the negative gate bias depletes the IZO channel, lowering the mobility and photoconductive gain. The photocurrent is shown to be linearly proportional to source-drain bias V_{DS} (**Figure 3.18**), complying to the relation[16] $I_{ph} = q*A*G_0*\tau_{trap}/\tau_{transit} = q*A*G_0*\tau_{trap}(\mu*V_{DS}/L^2)$, where A is the photosensor area, G_0 is the generation rate, μ is the effective field-effect mobility in the IZO channel, and L is the channel length. The transit time $\tau_{transit}$ can be reduced by decreasing the channel length, or increasing the mobility or source-drain bias. The lower bound for τ_{trap} is the carrier lifetime in **Figure 3.15(b)**. Compared to the device without camphor, the phototransistor with camphor retains trapped holes longer, leading to higher EQE across the spectral range.

Higher V_{GS} increases EQE but also the dark current noise as seen in **Figure 3.17(c)**. There is negligible difference in dark current between devices with or without camphor in the BHJ, indicating that noise is dominated by the shot noise in the transport channel, which is the same for both types of devices. For comparison, infrared photodiodes operating without an external bias are dominated by thermal noise.[4] However, here the devices are under bias, and shot noise or flicker noise can overtake the thermal noise component depending on the operational bias and frequency. The measured noise in the accumulation regime (V_{GS}= 0 V) is almost two orders of magnitude higher

than in the depletion regime (V_{GS}= -10 V), as shot noise[38] is proportional to the square root of current density.

The highest signal-to-noise ratio, or detectivity, is observed at the turn-on voltage in the dark, namely, at V_{GS}= -10 V in Figure 1(d). The specific detectivity[38] is $D^* = (A^*\Delta f)^{0.5}/NEP = (A^*\Delta f)^{0.5}(R/i_{noise})$, where A is the photosensor area, Δf is the temporal bandwidth, and NEP is the noise-equivalent power defined as responsivity R divided by noise current i_{noise}. **Figure 3.17(d)** displays the specific detectivity and noise-equivalent power calculated using measurement values from Figures 3(a) and 3(b). The best detectivity is obtained from the phototransistor with camphor operating in the depletion regime at V_{GS}= -10 V, and this device shows detectivity that surpasses commercial germanium photodiode (818-IR, Newport Corporation) in the IR region between 800 nm to 1300 nm, depending on light power as shown in **Figure 3.19**.

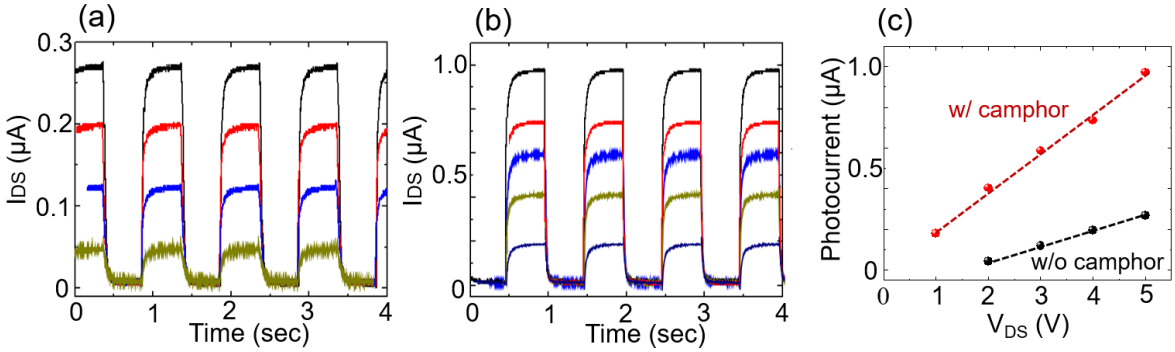

Figure 3.18. Temporal response of phototransistor (a) without and (b) with camphor under 940 nm light at 1 Hz modulating frequency. V_{DS} increases from 1 V with the step of 1 V. (c) Photocurrent versus V_{DS}.

3.4.3. Characteristics with Respect to The Incident Light Power

Another metric for photodetector is the dynamic range, which indicates the range of incident light power that the photodetector can response to and is defined as DR = 20 $\log(P_{inc,max}/P_{inc,min})$, where $P_{inc,max}$ is the maximum light power before saturation, and $P_{inc,min}$ is the minimum light power detectable above noise level. From **Figure 3.19(a)**, the dynamic range is estimated to be 127 dB for the phototransistor with camphor and 116 dB for the device without camphor. The superior dynamic range in the device with camphor is due to the lower detection limit from higher photoconductive gain. In both devices, the photoconductive gain leads to a non-constant responsivity versus incident light power in **Figure 3.19**, which contrasts with typical photodiodes in which responsivity remains constant with incident light power. In phototransistors, as the incident light power increases, the responsivity decreases because of the distribution of trap states.[22] The photogenerated carriers occupy deep traps first under low light power. The charges in deep traps are slow to escape from the traps due to high activation energy E_a, leading to long τ_{trap} and high photoconductive gain and responsivity. Under high light power, the deep trap states are already filled and shallow trap states start to dominate the photodetector response. The shallow traps allow faster de-trapping kinetics, resulting in lower τ_{trap} and reduced responsivity. Comparisons between devices with photoconductive gain need to take the light intensity into account; some of the reported high responsivity

values and thus high resolution will be valid only at low light levels. As such, the phototransistors are more sensitive at lower incident light power.

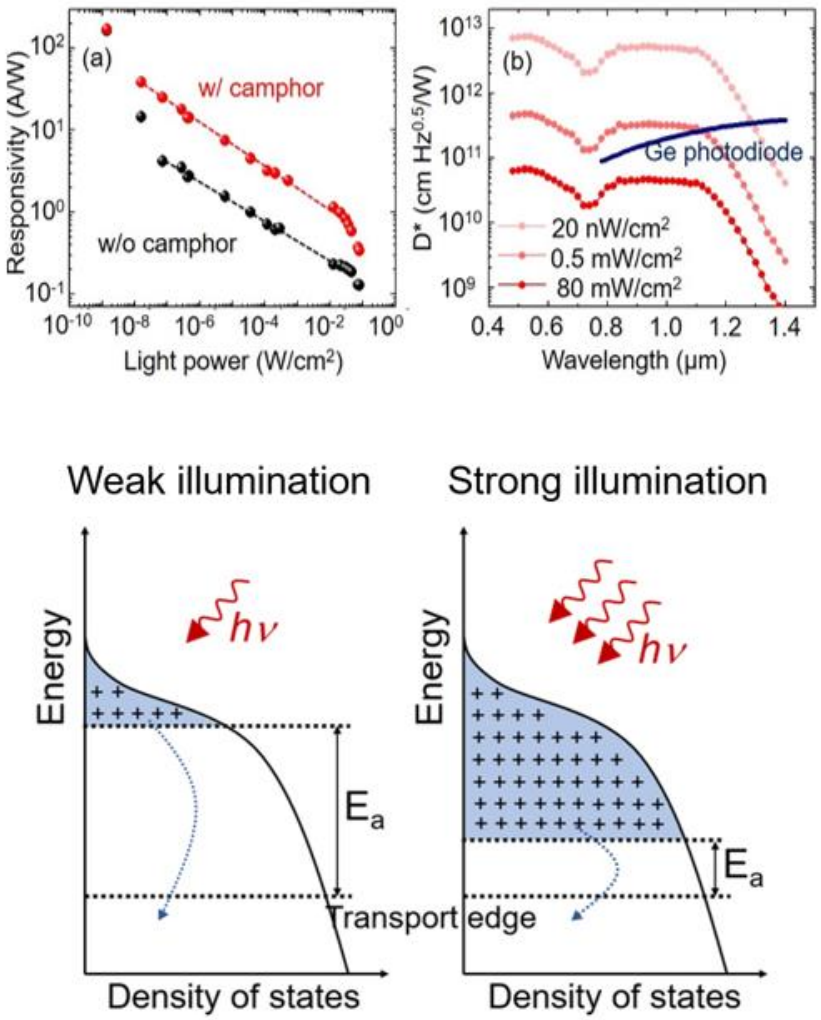

Figure 3.19. (a) Responsivity and (b) detectivity as a function of incident light power. The phototransistor is biased at V_{GS}= -10 V, V_{DS}= 5 V, and the light source is modulated at 10 Hz from a LED at 940 nm wavelength. The blue line indicates commercial germanium photodiode. (c) Schematic diagram of trap occupancy under different light power.

3.5 Conclusions

The phototransistors here achieve high-performance, broadband spectral response through the effective combination of BHJ for photogeneration and IZO for charge transport. This bilayer design allows independent optimization of each layer. The BHJ is improved with high-permittivity camphor to increase the trapped carrier lifetime, while the IZO layer maintains short carrier transit time. The photogeneration layer can be tuned by using different photosensitive polymers for different spectral ranges, and this work uses an infrared-sensitive polymer that is responsive in the visible to the infrared, from 500 nm to 1400 nm.

We examine the device characteristics with respect to operational frequency, applied bias, and incident light intensity, to analyze the dependence of photoconductive gain on these three factors. The devices show peak performance at low light intensity, with the applied gate bias in depletion regime near the turn-on voltage, and at switching frequencies that allow sufficient time for electron recirculation to maximize photoconductive gain. By understanding these dependence, the phototransistor noise is minimized, and the devices are shown to achieve detectivity up to 5 $x10^{12}$ $cmHz^{0.5}/W$ under incident light of 20 nW/cm^2 and allow operation at video-frame rate of 50 Hz. This excellent performance shows that the sosluble-processed infrared phototransistors here provide a path to realize affordable large-area infrared imagers crucial to many spectroscopic applications.

Chapter 3, in part, are the reprint of the material submitted for publication: Hyonwoong Kim, Zhenghui Wu, Naresh Eedegurala, Jason D. Azoulay, and Tse Nga Ng, “Solution Processed Phototransistors Combining Organic Absorber and Charge Transporting Oxide for Visible to Infrared Light Detction”, The dissertation author was the primary author of the paper.

3.6 References

[1] K. J. Baeg, M. Binda, D. Natali, M. Caironi, Y. Y. Noh, *Adv. Mater.* **2013**, *25*, 4267.

[2] D. J. Naczynski, M. C. Tan, M. Zevon, B. Wall, J. Kohl, A. Kulesa, S. Chen, C. M. Roth, R. E. Riman, P. V Moghe, *Nat. Commun.* **2013**, *4*, 2199.

[3] G. Hong, S. Diao, J. Chang, A. L. Antaris, C. Chen, B. Zhang, S. Zhao, D. N. Atochin, P. L. Huang, K. I. Andreasson, C. J. Kuo, H. Dai, *Nat. Photonics* **2014**, *8*, 723.

[4] Z. Wu, Y. Zhai, H. Kim, J. D. Azoulay, T. N. Ng, *Acc. Chem. Res.* **2018**, *51*, 3144.

[5] D. Kufer, G. Konstantatos, *ACS Photonics* **2016**, *3*, 2197.

[6] A. Rogalski, in *Proc. SPIE 10433*, **2017**, p. doi: 10.1117/12.2300779.

[7] J. A. Carr, D. Franke, J. R. Caram, C. F. Perkinson, M. Saif, V. Askoxylakis, M. Datta, D. Fukumura, R. K. Jain, M. G. Bawendi, O. T. Bruns, *Proc. Natl. Acad. Sci.* **2018**, *115*, 4465.

[8] F. P. G. de Arquer, A. Armin, P. Meredith, E. H. Sargent, *Nat. Rev. Mater.* **2017**, *2*, 16100.

[9] L. Dou, Y. Liu, Z. Hong, G. Li, Y. Yang, *Chem. Rev.* **2015**, *115*, 12633.

[10] L. Shen, Y. Lin, C. Bao, Y. Bai, Y. Deng, M. Wang, T. Li, Y. Lu, A. Gruverman, W. Li, J. Huang, *Mater. Horizons* **2017**, *4*, 242.

[11] J. Benduhn, K. Tvingstedt, F. Piersimoni, S. Ullbrich, Y. Fan, M. Tropiano, K. A. McGarry, O. Zeika, M. K. Riede, C. J. Douglas, S. Barlow, S. R. Marder, D. Neher, D. Spoltore, K. Vandewal, *Nat. Energy* **2017**, *2*, 17053.

[12] M. Stolterfoht, A. Armin, S. Shoaee, I. Kassal, P. Burn, P. Meredith, *Nat. Commun.* **2016**, *7*, 11944.

[13] W. Zhenghui, Y. Weichuan, L. A. E., A. J. D., N. T. Nga, *Adv. Funct. Mater.* **2018**, *28*, 1800391.

[14] R. D. Jansen-van Vuuren, A. Armin, A. K. Pandey, P. L. Burn, P. Meredith, *Adv.*

Mater. **2016**, *28*, 4766.

[15] H. Xu, J. Li, B. H. K. Leung, C. C. Y. Poon, B. S. Ong, Y. Zhang, N. Zhao, *Nanoscale* **2013**, *5*, 11850.

[16] A. Pierre, A. Gaikwad, A. C. Arias, *Nat. Photonics* **2017**, *11*, 193.

[17] Y. S. Rim, Y. M. Yang, S. Bae, H. Chen, C. Li, M. S. Goorsky, Y. Yang, *Adv. Mater.* **2015**, *27*, 6885.

[18] P. C. Y. Chow, N. Matsuhisa, P. Zalar, M. Koizumi, T. Yokota, T. Someya, *Nat. Commun.* **2018**, *9*, 4546.

[19] Y. J. Tak, D. J. Kim, W. G. Kim, J. H. Lee, S. J. Kim, J. H. Kim, H. J. Kim, *ACS Appl. Mater. Interfaces* **2018**, *10*, 12854.

[20] Y. Zhang, Y. Yuan, J. Huang, *Adv Mater* **2017**, *29*, 1603969.

[21] C. Xie, P. You, Z. Liu, L. Li, F. Yan, *Light Sci. &Amp; Appl.* **2017**, *6*, e17023.

[22] J. Jiang, C. Ling, T. Xu, W. Wang, X. Niu, A. Zafar, Z. Yan, X. Wang, Y. You, L. Sun, J. Lu, J. Wang, Z. Ni, *Adv Mater* **2018**, e1804332.

[23] G. Konstantatos, M. Badioli, L. Gaudreau, J. Osmond, M. Bernechea, F. P. G. de Arquer, F. Gatti, F. H. L. Koppens, *Nat. Nanotechnol.* **2012**, *7*, 363.

[24] J. Han, D. Yang, D. Ma, W. Qiao, Z. Y. Wang, *Adv. Opt. Mater.* **2018**, *6*, 1800038.

[25] M. M. Furchi, D. K. Polyushkin, A. Pospischil, T. Mueller, *Nano Lett* **2014**, *14*, 6165.

[26] Z. Wu, Y. Zhai, W. Yao, N. Eedugurala, S. Zhang, L. Huang, X. Gu, J. D. Azoulay, T. N. Ng, *Adv. Funct. Mater.* **2018**, 1805738.

[27] S. Leblebici, J. Lee, A. Weber-Bargioni, B. Ma, *J. Phys. Chem. C* **2017**, *121*, 3279.

[28] H. Kim, T. N. Ng, *Adv. Electron. Mater.* **2018**, *4*, 1700631.

[29] R. A. Street, T. N. Ng, R. A. Lujan, I. Son, M. Smith, S. Kim, T. Lee, Y. Moon, S. Cho, *ACS Appl. Mater. Interfaces* **2014**, *6*, 4428.

[30] S. Jeon, S. E. Ahn, I. Song, C. J. Kim, U. I. Chung, E. Lee, I. Yoo, A. Nathan, S. Lee, J. Robertson, K. Kim, *Nat. Mater.* **2012**, *11*, 301.

[31] T. N. Ng, D. E. Schwartz, P. Mei, S. Kor, J. Veres, P. Bröms, C. Karlsson, *Flex. Print. Electron.* **2016**, *1*, 015002.

[32] G. L. Whiting, D. E. Schwartz, T. N. Ng, B. S. Krusor, R. Krivacic, A. Pierre, A. C. Arias, M. Harting, D. van Buren, K. L. Short, *Flex. Print. Electron.* **2017**, *2*, 034002.

[33] Z. Wu, W. Yao, A. E. London, J. D. Azoulay, T. N. Ng, *ACS Appl. Mater. Interfaces* **2017**, *9*, 1654.

[34] T. N. Ng, M. L. Chabinyc, R. A. Street, A. Salleo, in *IEEE Int. Reliab. Phys. Symp.*, Phoenix, **2007**, pp. 243–247.

[35] J. Bisquert, L. Bertoluzzi, I. Mora-Sero, G. Garcia-Belmonte, *J. Phys. Chem. C* **2014**, *118*, 18983.

[36] I. Constantinou, X. Yi, N. T. Shewmon, E. D. Klump, C. Peng, S. Garakyaraghi, C. K. Lo, J. R. Reynolds, F. N. Castellano, F. So, *Adv. Energy Mater.* **2017**, *7*, 1601947.

[37] D. Macdonald, A. Cuevas, *Appl. Phys. Lett.* **1999**, *74*, 1710.

[38] A. Rogalski, Z. Bielecki, *Bull. Polish Acad. Sci. Tech. Sci.* **2004**, *52*, 43.